Improved Computational Modeling of the Kinetics of the Acetylperoxy + HO_2 Reaction

Journal:	*Faraday Discussions*
Manuscript ID	FD-ART-02-2022-000030.R2
Article Type:	Paper
Date Submitted by the Author:	14-Apr-2022
Complete List of Authors:	Kuwata, Keith; Macalester College, Department of Chemistry DeVault, Marla; University of Colorado Boulder, Chemistry Department Claypool, Duncan; University of Illinois College of Medicine

Improved Computational Modeling of the Kinetics of the Acetylperoxy + HO_2 Reaction

Keith T. Kuwata,[*] Marla P. DeVault,[†] and Duncan J. Claypool[‡]

Department of Chemistry, Macalester College, Saint Paul, Minnesota 55105-1899

---

[*] Corresponding author. Tel: (651) 696-6768; Fax: (651) 696-6432; e-mail: kuwata@macalester.edu

[†] Current address: Department of Chemistry, University of Colorado Boulder, Boulder, CO 80309-0215

[‡] Current address: University of Illinois College of Medicine at Chicago, Chicago, IL 60612-7332

ABSTRACT

The acetylperoxy + HO_2 reaction has multiple impacts on the troposphere, with a triplet pathway leading to peracetic acid + O_2 (reaction 1a) competing with singlet pathways leading to acetic acid + O_3 (reaction 1b) and acetoxy + OH + O_2 (reaction 1c). A recent experimental study has reported branching fractions for these three pathways (α_{1a}, α_{1b}, and α_{1c}) from 229 K to 294 K. We constructed a theoretical model for predicting α_{1a}, α_{1b}, and α_{1c} using quantum chemical and Rice-Ramsperger-Kassel-Marcus/master equation (RRKM/ME) simulations. Our main quantum chemical method was Weizmann-1 Brueckner Doubles (W1BD) theory; we combined W1BD and equation-of-motion spin-flip coupled cluster (SF) theory to treat open-shell singlet structures. Using RRKM/ME simulations that included all conformers of acetylperoxy-HO_2 pre-reactive complexes led to a 298 K triplet rate constant, $k_{1a} = 5.11 \times 10^{-12}$ cm^3 molecule^{-1} s^{-1}, and values of α_{1a} in excellent agreement with experiment. Increasing the energies of all singlet structures by 0.9 kcal mol^{-1} led to a combined singlet rate constant, $k_{1b+1c} = 1.20 \times 10^{-11}$ cm^3 molecule^{-1} s^{-1}, in good agreement with experiment. However, our predicted variations in α_{1b} and α_{1c} with temperature are not nearly as large as those measured, perhaps due to the inadequacy of SF theory in treating the transition structures controlling acetic acid + O_3 formation *vs.* acetoxy + OH + O_2 formation.

INTRODUCTION

The unimolecular and bimolecular reactions of organic peroxy radicals (RO_2) impact tropospheric chemistry in multiple ways.[1] The decrease in NO_x concentrations over urban areas in recent years[2] has heightened the importance of RO_2 reactions with other peroxy radicals, including hydroperoxy (HO_2).[3] The acetylperoxy ($CH_3C(O)OO$) + HO_2 reaction is especially rich mechanistically in that radical termination via hydroperoxide formation on the triplet surface (reaction 1a) competes with acetic acid and ozone formation (reaction 1b) and OH formation (reaction 1c), both on the singlet surface.

$$CH_3C(O)OO + HO_2 \rightarrow CH_3C(O)OOH + O_2 \quad [1a]$$

$$CH_3C(O)OO + HO_2 \rightarrow CH_3C(O)OH + O_3 \quad [1b]$$

$$CH_3C(O)OO + HO_2 \rightarrow CH_3C(O)O + OH + O_2 \quad [1c]$$

Several experimental measurements[4-8] of room-temperature branching fractions (α_i; i = 1a, 1b, or 1c) over the past 15 years have been broadly consistent with one another, with $\alpha_{1a} = 0.2$-0.4, $\alpha_{1b} = 0.1$-0.2, and $\alpha_{1c} = 0.5$-0.6. These branching fractions do not vary in a statistically significant way with pressure from 100 Torr[4] to 800 Torr.[8]

A previous theoretical study by Hasson et al.[9] provided a mechanism (excerpted in Figure 1) that reproduced the experimental branching fractions at 1 atm. This mechanism supported the earlier contention[10] that the singlet pathways proceed through a hydrotetraoxide intermediate **10**. However, the CBS-QB3 quantum chemical method[11] used in the study predicted that the singlet pre-reactive complex **8** is ~7 kcal mol^{-1} more stable than the triplet pre-reactive complex **3** and that lowering the energy of **8** by an additional 1 kcal mol^{-1} was necessary to reproduce experimental yields. For a number of theoretical reasons we will discuss below, we find the large differences in the energies of **3** and **8** to be dubious. Moreover, Rice-Ramsperger-Kassel-Marcus/master equation simulations[9] revealed that complex **8** is prone to collisional stabilization, giving rise to a pressure dependence in branching fractions inconsistent with experiment.[4, 8] Finally, the predicted total rate constant (in cm^3 $molecule^{-1}$ s^{-1} at 298 K) for the $CH_3C(O)OO$ + HO_2 reaction, 4 x 10^{-12}, is a factor of 5 lower than the IUPAC[12] and JPL[13] recommended value of 1.4 x 10^{-11}.

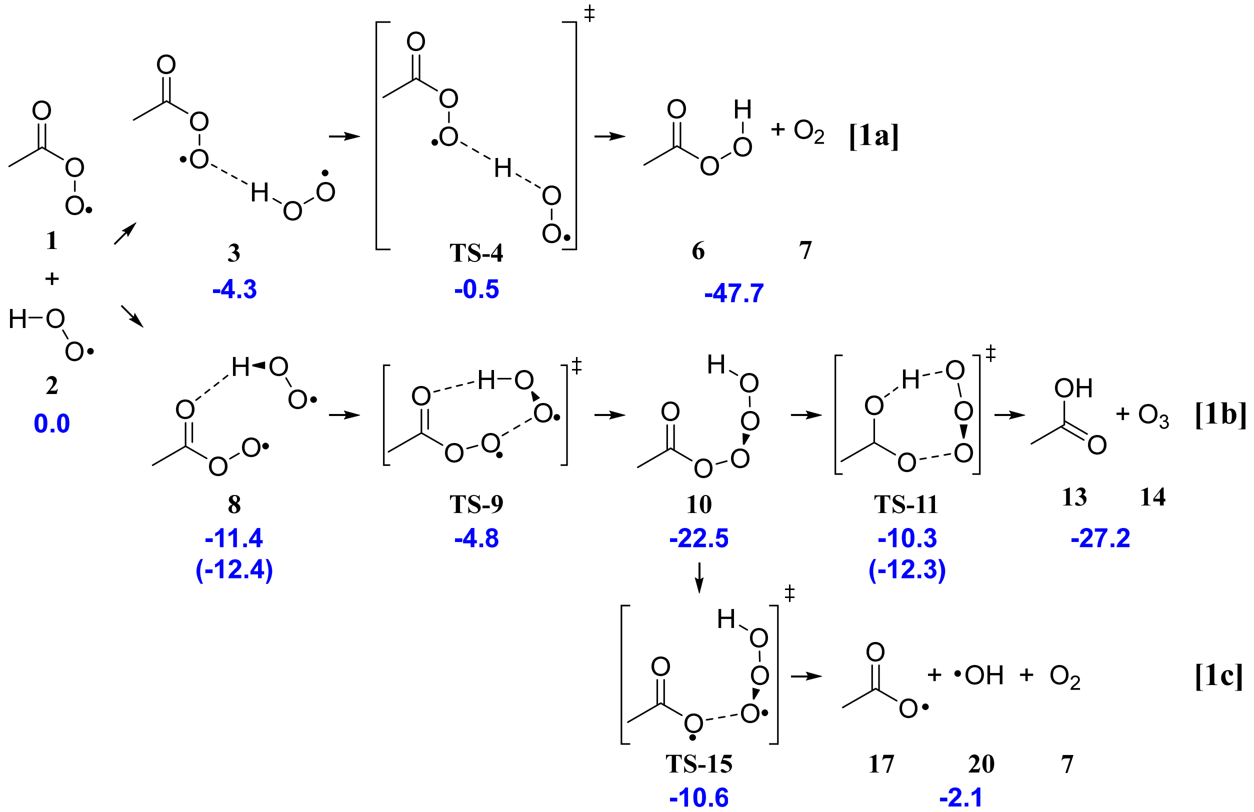

Figure 1. Mechanism for the acetylperoxy + HO_2 reaction from Hasson et al.[9] with exit-channel complexes omitted. Relative energies at 0 K in kcal mol^{-1} in blue from CBS-QB3 calculations; adjusted energies used to reproduce experimental 1-atm branching fractions in parentheses.

The shortcomings in the previous theoretical work[9] coupled with the recent temperature-dependent kinetic data of Hui et al.[4] inspire the theoretical re-examination of the acetylperoxy + HO_2 reaction presented in this paper. We improve the accuracy of the theoretical modeling in two ways. First, we use more rigorous electronic structure methods, W1BD[14] and equation-of-motion coupled cluster theory,[15, 16] for the open-shell singlet diradical structures in the mechanism. These methods should provide more accurate energetics than CBS-QB3 for such species.[17, 18] Second, we include all conformers of the minima and transition structures in our statistical rate theory calculations. Explicit treatment of all energetically relevant conformers can be critical for obtaining highly accurate predictions for peroxy radical reactions.[19]

COMPUTATIONAL METHODS

Electronic Structure Calculations. We calculated the zero-point-corrected electronic energies of most minima and transition structures using W1BD, the variant of Weizmann-1 theory employing Brueckner orbitals.[14] W1BD theory involves extrapolations of the BDRef, BD, and BD(T) energies to their complete basis set limits. All W1 methods employ the B3LYP/cc-pVTZ+d model chemistry[20-22] to obtain optimized geometries and harmonic vibrational frequencies. As judged by the G2/97 dataset, W1 theory is almost as accurate with B3LYP/cc-pVTZ+d geometries as with CCSD(T)/cc-pVQZ+d geometries.[23] We used the default scaling factor[23] of 0.985 to correct the B3LYP/cc-pVTZ+d harmonic frequencies in the computation of zero-point vibrational energies.

We adapted W1BD theory for open-shell-singlet (OSS) diradical minima (*e.g.* different conformers of **8** in Figure 1 above) by using broken-spin-symmetry (BSS) wave functions[24] in the computation of B3LYP geometries and frequencies and in the evaluation of the BDRef, BD, and BD(T) energies. (We denote this adaptation as UW1BD theory.) BSS density functional theory methods can predict accurate geometries and frequencies for organic diradicals.[25] Moreover, the unrestricted UW1BD method is less prone to spin contamination than other W1 methods for open-shell species[14] that lack strongly multireference character. We took the same approach for the transition structures responsible for interconverting the diradical minima and for the concerted cycloreversion transition structure, **TS-11**, leading to acetic acid + ozone (Figure 1 above).

We validated our application of (U)W1BD theory to peroxy radicals by comparing our predictions for the HO_2 + HO_2 reaction to the rigorous CCSD(T)/CBS and MRCI+Q calculations of Sprague and Irikura.[26] As depicted in Figure S1 of the Supporting Information, we predict the energies of $(HO_2)_2$ triplet and OSS radical pairs relative to the closed-shell singlet (CSS) HO_4H tetraoxide to within 1 kcal mol^{-1} of the previously reported values.[26]

There was a problem with our (U)W1BD//B3LYP treatment of the reaction mechanism in one region of the singlet and triplet potential energy surfaces, as represented by the stationary points rendered in Figure 2. On the singlet surface, **TS-8eg**, which interconverts acetylperoxy-HO_2 complex isomers **8e** and **8g**, has a lower UW1BD//B3LYP energy than **8e**. Likewise, on the triplet surface, **TS-3eg** has a lower W1BD//B3LYP energy than **3e**. Neither re-optimization of the TS location using the IRCMax approach[27] nor re-computation of zero-point energies using anharmonic frequencies corrected this unphysical artifact. In the simulations described in the next section, we arbitrarily set the interconversion barriers to be 0.01 kcal mol^{-1} above the energy of **3e** and **8e**.

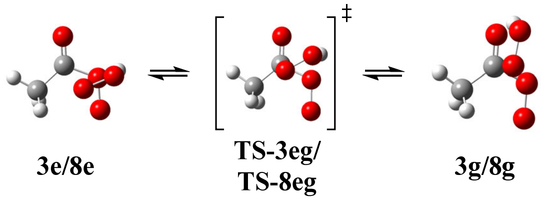

Figure 2. Problematic part of the pre-reactive complex conformational space as described by (U)W1BD//B3LYP theory.

Finally, **TS-9** and **TS-15** (Figure 1 above) contain significant amounts of both dynamic and static electron correlation, as they involve transitions between OSS and CSS minima. We took the following approach to modeling these structures: (1) We obtained optimized geometries and harmonic vibrational frequencies using the ωB97X-D/cc-pVTZ+d model chemistry, scaling the harmonic frequencies by 0.975 to obtain zero-point energy corrections.[28] The ωB97X-D density functional,[29] which explicitly treats dispersion interactions, should provide more accurate transition structure geometries than B3LYP.[30] (2) We followed the approach of Sprague and Irikura,[26] Pfeifle et al.,[31] and Kuwata et al.[32] by combining two different methods to calculate the electronic energy of these OSS species: $E(\text{OSS}) = {}^3E(\text{W1BD}) + \Delta E_{\text{SF}}$. The ${}^3E(\text{W1BD})$ term is the W1BD electronic energy of a particular conformer of **TS-9** or **TS-15** treated as a triplet. Given that a triplet state is largely single-reference in character, a composite single-reference method like W1BD should provide a very accurate triplet energy, capturing most of the dynamic electron correlation present in the species. The ΔE_{SF} term is the singlet-triplet energy gap for the same particular conformer of **TS-9** or **TS-15** computed with equation-of-motion spin-flip coupled-cluster theory[15] with a perturbative treatment of triple excitations[16] (EOM-SF-CCSD(dT) theory). Spin-flip (SF) theory allows one to construct the wave function for an OSS by applying a complete set of spin-flipping excitations to a high-spin triplet state that is accurately described by a single-reference method like CCSD(dT).[33, 34] SF theory captures much of the static electron correlation in the electronic structure of a species with modestly-sized basis sets;[35] we computed the SF singlet-triplet gaps with the 6-311G* basis set. In many of the conformers of **TS-9** and **TS-15**, the local maximum in the $E(\text{OSS}) = {}^3E(\text{W1BD}) + \Delta E_{\text{SF}}$ energy did not coincide with the ωB97X-D/cc-pVTZ+d saddle point, requiring an IRCMax adjustment, as we discuss below. Finally, in order to collate a self-consistent set of relative energies for the entire mechanism, we performed both

W1BD and *E*(OSS) calculations on singlet diradical pair **8b** (Figure 6 below); that is, the *E*(OSS) energies reported for the conformers of **TS-9** and **TS-15** are all relative to the *E*(OSS) energy of **8b**.

We used Gaussian 16[36] for all of the quantum chemical calculations reported here except for the singlet-triplet gaps computed with EOM-SF-CCSD(dT) theory. For the latter calculations, we used Q-Chem 5.2.[37]

Statistical Rate Theory Calculations. We used MultiWell-2019[38-40] to solve the one-dimensional energy-based master equation (ME) for the acetylperoxy + HO_2 reaction mechanism. The 0 K energies of all species in the simulations came from the calculations described in the previous section. We applied Rice-Ramsperger-Kassel-Marcus (RRKM) theory[41] to determine microcanonical rate constants, *k*(*E*), for reactions with tight transition states:

$$k\left(E\right)=\frac{m^{\ddagger}}{m}\frac{\sigma_{\mathrm{ext}}}{\sigma_{\mathrm{ext}}^{\ddagger}}\frac{g_{\mathrm{e}}^{\ddagger}}{g_{e}}\frac{G^{\ddagger}\left(E-E_{\mathrm{o}}\right)}{h\rho\left(E\right)} \qquad [2]$$

In equation 2, variables with the double dagger ‡ describe the transition state and variables without the ‡ describe the reactant. The variable *m* is the number of optical isomers, σ is the external rotation symmetry number, g_e is the electronic degeneracy, $G^{\ddagger}\left(E-E_{\mathrm{o}}\right)$ is the sum of states at the transition state, E_o is the zero-point corrected reaction barrier, *h* is Planck's constant, and $\rho\left(E\right)$ is the density of states of the reactant. We computed the requisite sums and densities of states under the rigid rotor-harmonic oscillator approximations based on the moments of inertia and vibrational frequencies computed either with B3LYP/cc-pVTZ+d or with ωB97X-D/cc-pVTZ+d, as described above.

We determined values of *k*(*E*) for the barrierless dissociation of acetylperoxy-HO_2 radical pairs using the following multi-step approach similar to what we have employed in previous studies:[32, 42] (1) We assumed the rate of formation of the acetylperoxy-HO_2 radical pairs to be governed by the sum of the dipole-dipole, dipole-quadrupole, dipole-induced dipole, and dispersion forces attracting the radicals to each other. We evaluated the capture rate constant, k_{cap}, using the long-range transition state theory analytical formulas derived by Georgievskii and Klippenstein;[43] we performed a natural bond order analysis[44] of the CCSD/MG3[45, 46] density to compute the requisite dipole moments, quadrupole moments, polarizabilities, and vertical ionization energies. The Supporting Information contains more details about these calculations. (2) We calculated the equilibrium constants, K_{eq}, for the dissociation of the radical pairs into free acetylperoxy and HO_2 radicals. The calculations, performed with the Thermo program of the MultiWell program suite,[38] employed W1BD zero-point-corrected electronic energies and B3LYP/cc-pVTZ+d partition functions. (3) Using detailed balance, we determined the high-pressure-limit rate constants, k_{dissoc}, for the dissociation of a given radical pair: $k_{\mathrm{dissoc}} = K_{\mathrm{eq}}k_{\mathrm{cap}}$. (4) Using the inverse Laplace transform function in MultiWell, we converted k_{dissoc} values into the $k(E)$ values needed for the ME simulations.

The bath gas in our simulations was N_2, with Lennard-Jones parameters of $\sigma = 3.74$ Å and $\varepsilon/k_B = 82$ K.[47, 48] Using the same methodology[49-52] described in earlier work,[53] we estimated Lennard-Jones parameters of $\sigma = 7.721$ Å and $\varepsilon/k_B = 336.9$ K for all acetylperoxy-HO_2 adducts. We used the exponential-down model to describe collisional stabilization, using an energy grain size of 10 cm^{-1} and assuming an average, temperature-independent energy lost per collision of 300 cm^{-1}, a typical value in ME simulations.[54] We ran each simulation for 1000 collisions to ensure that the simulation had reached the pseudo steady state;[55] in practice, the populations and vibrational energies of all of the species in a given simulation would converge by 300 collisions at the most. We ran trials at pressures from 1 Torr to 760 Torr. Each reported pseudo-steady state yield is the average result from 10^8 Monte Carlo simulations. This gave an uncertainty of roughly ±1 x 10^{-5} for fractional yields on the order of 1 and roughly ±1 x 10^{-8} for fractional yields on the order of 10^{-8}.

RESULTS AND DISCUSSION

Quantum Chemical Results. *Triplet Pathway*. Figure 3 presents highlights of our W1BD//B3LYP prediction for reaction 1a, the pathway on the triplet surface leading to peracetic acid (**6**) and triplet O_2 (**7**). The conformer of $CH_3C(O)OO$ with synperiplanar C=O and O-O bonds, **1-*syn***, reacts with HO_2 (**2**) *via* the formation of two pre-reactive complexes, **3a** and **3f**. In **3a**, the HO_2 forms a hydrogen bond to the carbonyl O, while in **3f**, the HO_2 forms a hydrogen bond to the internal O of the peroxy group. The *anti* conformer of $CH_3C(O)OO$, **1-*anti***, reacts with HO_2 *via* the formation of pre-reactive complex **3h**, which, like **3a**, is held together by a hydrogen bond to the carbonyl O.

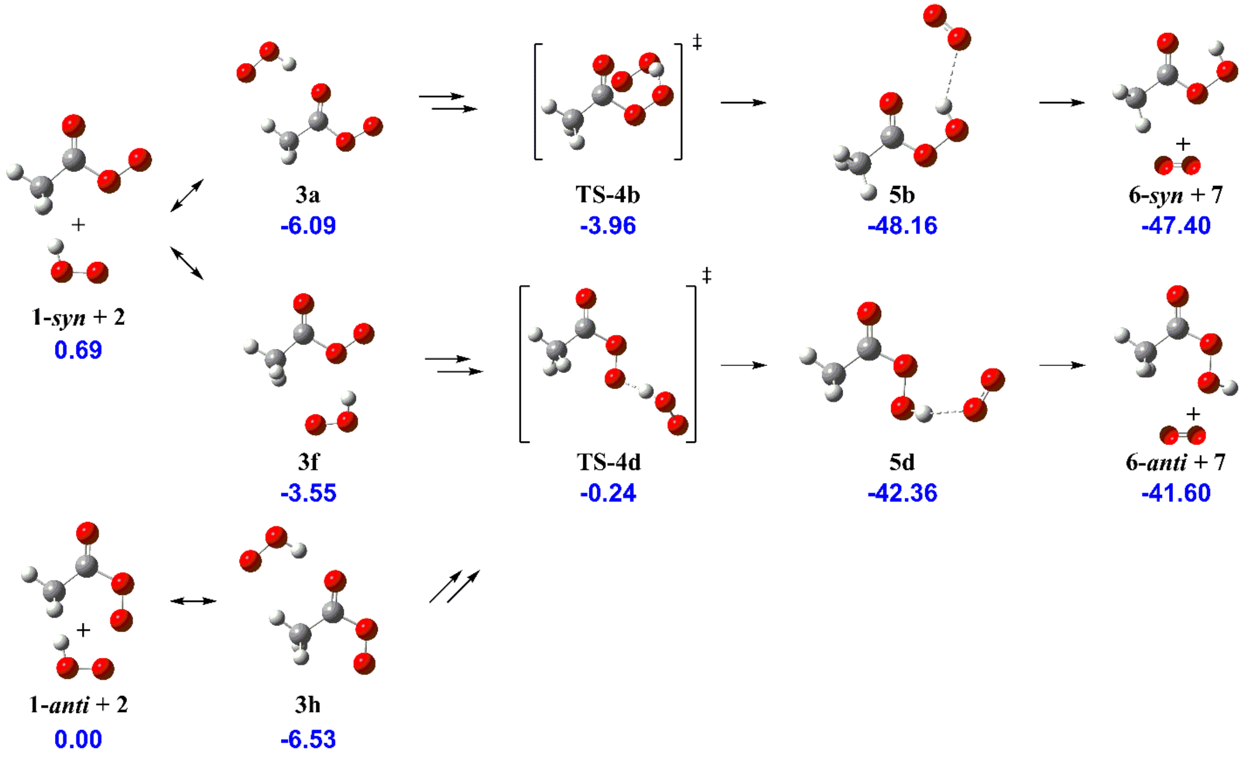

Figure 3. Highlights of the triplet pathway for the acetylperoxy + HO_2 reaction. Relative energies (0 K, kcal mol^{-1}) in blue from W1BD//B3LYP calculations. Double arrows denote that one or more structures have been omitted between the structures shown.

Extensive searching using B3LYP/cc-pVTZ+d calculations revealed a total of eight $CH_3C(O)OO$-HO_2 pre-reactive conformers along with their interconversion transition structures (Figure 4). Conformers **3a**, **3f**, and **3h** are the only three structures we located on the triplet surface formed directly from the acetylperoxy and HO_2 fragments. For each of the other five conformers, breaking of the hydrogen bond by scanning the H---O distance leads to another bound conformer. We repeated these intrafragment scans using a density functional, B3LYP-D3, which includes Grimme's empirical treatment of dispersion,[56] and the larger aug-cc-pVTZ basis set.[57] The changes in both density functional and basis set provide a more accurate description of intermolecular forces. However, the B3LYP-D3/aug-cc-pVTZ scans still indicated that only **3a**, **3f**, and **3h** are formed directly from $CH_3C(O)OO$ + HO_2.

Our current calculations notwithstanding, we cannot exclude the possibility that a more thorough characterization of the van der Waals region of the potential energy surface would reveal direct formation of other conformers. We discuss the impact of this possibility on the predicted kinetics below.

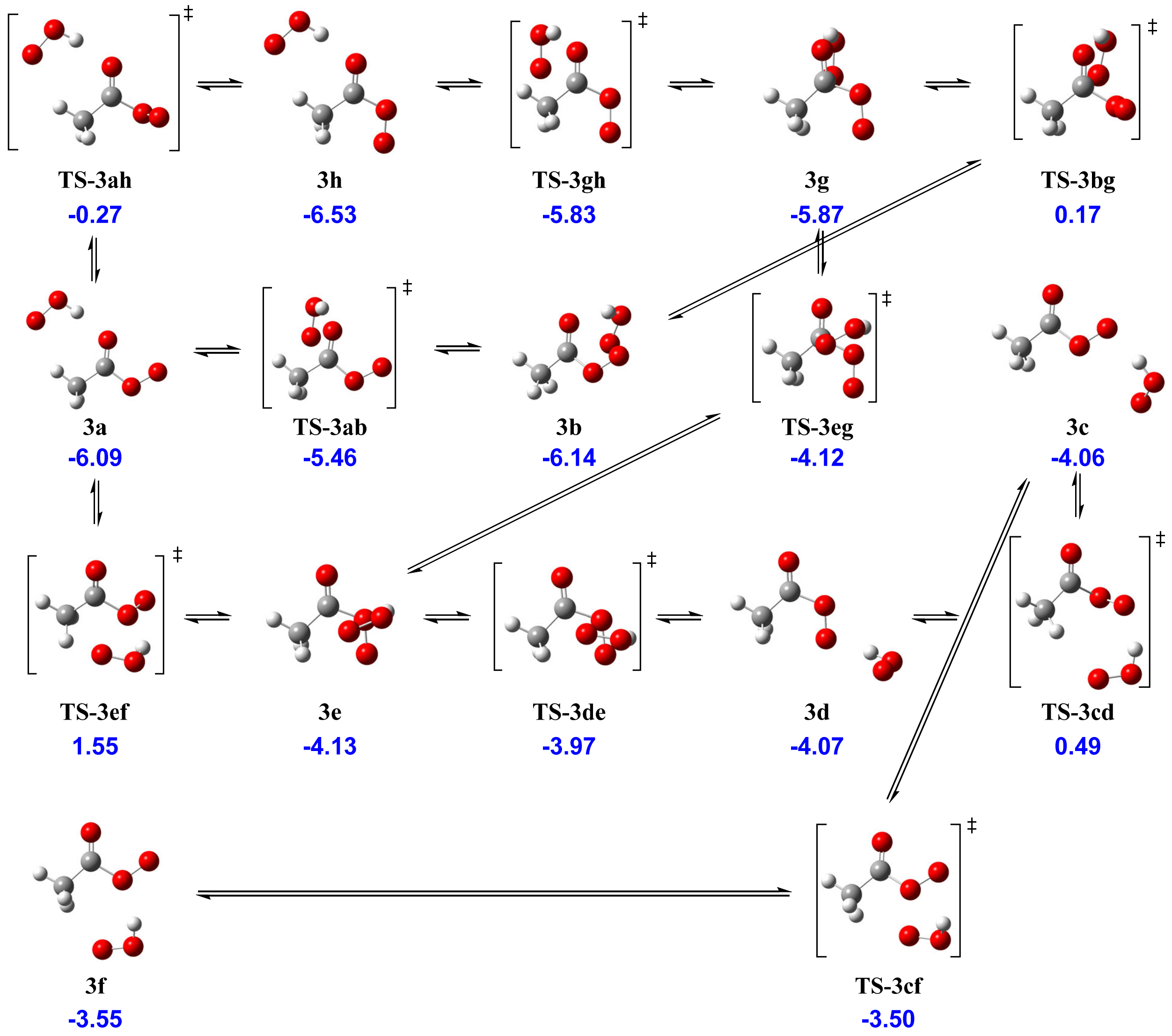

Figure 4. Triplet reactive complexes and interconversion transition structures for the acetylperoxy + HO_2 reaction. Energies (0 K, kcal mol^{-1}) in blue from W1BD//B3LYP calculations relative to the combined energies of *anti* acetylperoxy + HO_2.

Figure 4 reveals two categories of pre-reactive complex conformers. In one category (**3c**, **3d**, **3e**, and **3f**) , the binding energies are all ~ -4 kcal mol^{-1}; in the other category (**3a**, **3b**, **3g**, and **3h**), the binding energies are all ~ -6 kcal mol^{-1}. These two categories correspond to which acetylperoxy O is serving as the hydrogen bond acceptor; the magnitude of the partial charge on the O atom largely controls hydrogen bond strength (Figure 5).

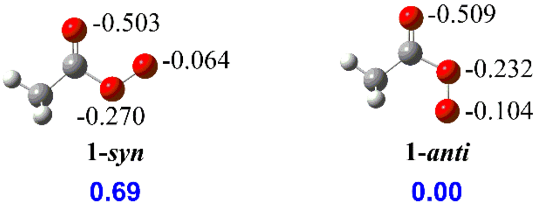

Figure 5. Selected CCSD/MG3 natural population analysis charges for the two conformers of the acetylperoxy radical. Relative energies (0 K, kcal mol^{-1}) in blue from W1BD//B3LYP calculations.

CCSD/MG3 natural population analysis (NPA) charges[58] are -0.5 for the carbonyl oxygen, but only -0.1 to -0.3 for the peroxy oxygens. Thus, the conformers with hydrogen bonds to the carbonyl O are all ~2 kcal mol^{-1} more stable than the other conformers. It is also worth noting that hydrogen bonding to the terminal peroxy O can be slightly more stabilizing than hydrogen bonding to the internal peroxy O in spite of the fact that the negative charge on the terminal O is smaller in magnitude. In particular, **3c** is ~0.5 kcal mol^{-1} more stable than **3f** (Figure 4 above). This may reflect lower steric repulsion in **3c**. A smaller factor in hydrogen bond strength is the relative orientation of the acetylperoxy C=O and O-O bonds. Conformer **1-*anti*** is 0.7 kcal mol^{-1} more stable than **1-*syn*** (Figure 5) due to an avoided repulsion between the carbonyl and terminal peroxy O atoms in the *anti* form. The complexes likewise manifest this preference (*e.g.* **3a** *vs*. **3h** in Figure 3), but the energetic preference for antiperiplanar C=O and O-O bonds is < 0.5 kcal mol^{-1} for the complexes.

With respect to the interconversion transition structures, Figure 4 again reveals two categories. **TS-3ab**, **TS-3de**, **TS-3cf**, **TS-3eg**, and **TS-3gh** are all within 1 kcal mol^{-1} of at least one of the minima immediately surrounding each of these TSs on the potential energy surface. Their imaginary frequencies all involve the movement of the HO_2 moiety from one hydrogen bond acceptor site to another. The other structures, **TS-3ah**, **TS-3bg**, **TS-3ef**, and **TS-3cd**, are all several kcal mol^{-1} higher in energy than their surrounding minima, and their imaginary frequencies all correspond to rotation about the acetylperoxy C-OO bond. These relatively high barriers have implications for the reaction dynamics, as we shall see below.

We found that the two original acetylperoxy conformers each can undergo intermolecular hydrogen atom transfer *via* **TS-4b** and **TS-4d** (Figure 3). The earlier theoretical study of Hasson et al.[9] identified only one hydrogen transfer transition structure resembling **TS-4d**. The TSs are submerged and lead to exit-channel complexes **5b** and **5d**, which in turn dissociate irreversibly to peracetic acid and O_2. Acid conformer **6-*syn*** is 6 kcal mol^{-1} lower in energy than **6-*anti*** due to the stabilizing intramolecular hydrogen bond in **6-*syn***.

Singlet Pathway. Figure 6 presents highlights of our predictions for the first part of the singlet pathway; that is, the formation of the hydrotetraoxide (**10b** and **10e**), while Figure S2 (in the Supporting Information) presents our UW1BD//B3LYP predictions for all eight conformers of the singlet pre-reactive complex, **8**, and their ten interconversion transition structures. The conformational landscapes of the singlet and triplet pre-reactive complexes (Figure 4 above) are very similar. There are three conformers whose formation initiate reactivity along the singlet pathway, two involving hydrogen bonding of HO_2 to acetylperoxy conformer **1-*syn*** and one involving hydrogen bonding to **1-*anti***. Hydrogen bonding to the carbonyl O of $CH_3C(O)OO$ stabilizes the pre-reactive complex by ~6 kcal mol^{-1} (*e.g.* **8a**), while hydrogen bonding to a peroxy O stabilizes the complex by only ~4 kcal mol^{-1} (*e.g.* **8f**). Finally, structures whose acetylperoxy moiety has antiperiplanar C=O and O-O bonds are ≤ 0.5 kcal mol^{-1} more stable than structures with synperiplanar C=O and O-O bonds (*e.g.* **8h** *vs*. **8a**). The high similarity of the triplet and singlet landscapes is due to the very weak interactions between the unpaired electrons on the acetylperoxy and HO_2 moieties. For example, in **8b**, EOM-SF-CCSD(dT)/6-311G* calculations predict a singlet-triplet gap of only 0.01 kcal mol^{-1}.

As we did for the triplet surface, we performed B3LYP-D3/aug-cc-pVTZ scans of the hydrogen bond (that is, systematically varying the O---H distance) for all singlet conformers and confirmed that only **8a**, **8f**, and **8h** form directly from acetylperoxy + HO_2. Again, a more exhaustive search of the van der Waals region of the potential energy surface could reveal the direct formation of additional singlet complex conformers. We discuss the impact of the possibility on reaction kinetics below.

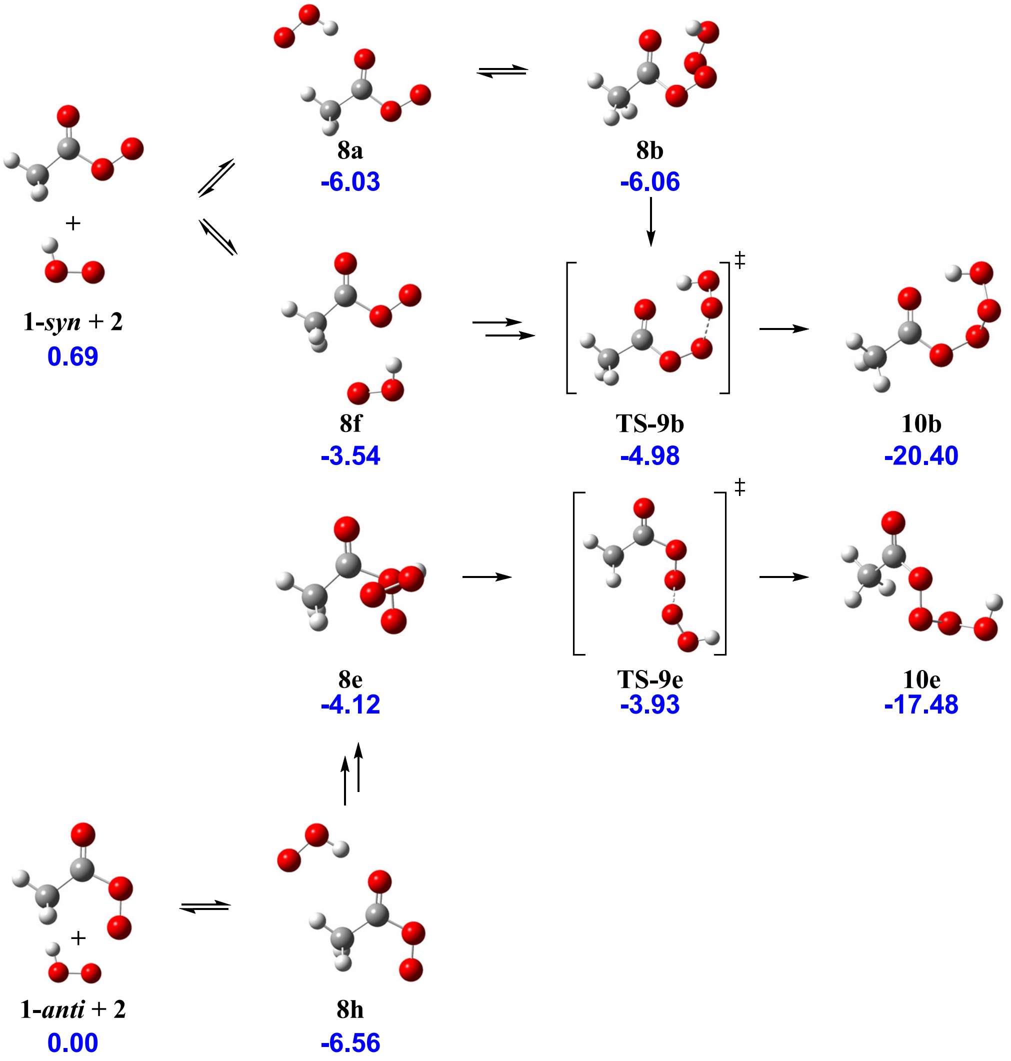

Figure 6. Highlights of the singlet pathway for the acetylperoxy + HO_2 reaction. Relative energies (0 K, kcal mol^{-1}) in blue from (U)W1BD//B3LYP and [^3E(W1BD) + ΔE_{SF}]//ωB97X-D calculations. Double arrows denote that one or more structures have been omitted between the structures shown.

We located transition structures for tetraoxide formation involving both the *syn* and *anti* conformers of acetylperoxy (**TS-9b** and **TS-9e**, respectively). As discussed above, the TS geometries come from ωB97X-D/cc-pVTZ+d calculations and the TS energies are given by

E(OSS) = ^3E(W1BD) + ΔE_{SF}. At the ωB97X-D/cc-pVTZ+d saddle point, the value of E(OSS) for **TS-9b** was below that of **8b** and the value of E(OSS) for **TS-9e** was below that of **8e**. We used the IRCMax approach[27] to adjust the barrier heights, computing the ^3E(W1BD) and ΔE_{SF} terms along the ωB97X-D/cc-pVTZ+d minimum energy paths predicted by the IRC method.

The current results differ significantly from those in Hasson et al.[9] (Figure 1 above). The previous work reported only one conformer of **8**, resembling our **8b**, and only one conformer of **TS-9**, resembling our **TS-9b**. More drastically, the CBS-QB3 energy of singlet pre-reactive complex **8** is 7 kcal mol^{-1} lower than that of triplet pre-reactive complex **3**. This difference in stability cannot be due to an attractive interaction between the unpaired electrons on the $CH_3C(O)OO$ and HO_2 moieties; as noted above, the singlet-triplet gap in **8b** is only 0.01 kcal mol^{-1}, indicating very weak coupling. The preferential stabilization of the singlet complex is probably an artifact of the spin contamination correction term in CBS-QB3 and related methods.[59] This term was derived to improve the accuracy of doublets, whose unrestricted Hartree-Fock (UHF) value of $\langle S^2 \rangle$ at equilibrium geometries rarely exceeds the ideal value of 0.75 by more than ~0.5. In contrastG, the singlet diradicals considered here have ideal $\langle S^2 \rangle$ values of exactly 0, but in practice have UHF $\langle S^2 \rangle$ values of ~1.0. We may therefore expect the CBS-QB3 method to overcompensate for spin contamination in singlet diradicals, as reported by Sirjean et al.[60] In the case of **8b**, the CBS-QB3 spin-contamination correction term is -6.13 kcal mol^{-1}.

We located eight hydrotetraoxide conformers and nine transition structures interconverting these conformers (Figure 7). The Z conformers (*i.e.*, those with synperiplanar C=O and CO-O bonds, **10b**, **10i**, **10k**, and **10n**, are all 18-20 kcal mol^{-1} lower in energy than the combined energies of separated *anti* acetylperoxy + HO_2 (**1-*anti* + 2**, Figure 6 above). The E conformers, **10e**, **10j**, **10l**, and **10m**, have antiperiplanar C=O and CO-O bonds and are all 16-17 kcal mol^{-1} lower in energy than **1-*anti* + 2**. The slightly greater stability of the *Z* conformers is characteristic of most esters[61] and is largely a consequence of the steric repulsion between the –CH_3 and the –OOOH groups in the *E* conformers. The most stable conformer, **10b**, is also stabilized by an intramolecular hydrogen bond to the carbonyl oxygen. The barriers to interconverting *E* and *Z* conformers range from 7 to 12 kcal mol^{-1}. These relatively large barriers to rotation, which arise from the loss of hyperconjugation between the two oxygen atoms bonded to the sp^2-hybridized carbon,[62] somewhat restrict the coupling between reaction channels, as we shall discuss below.

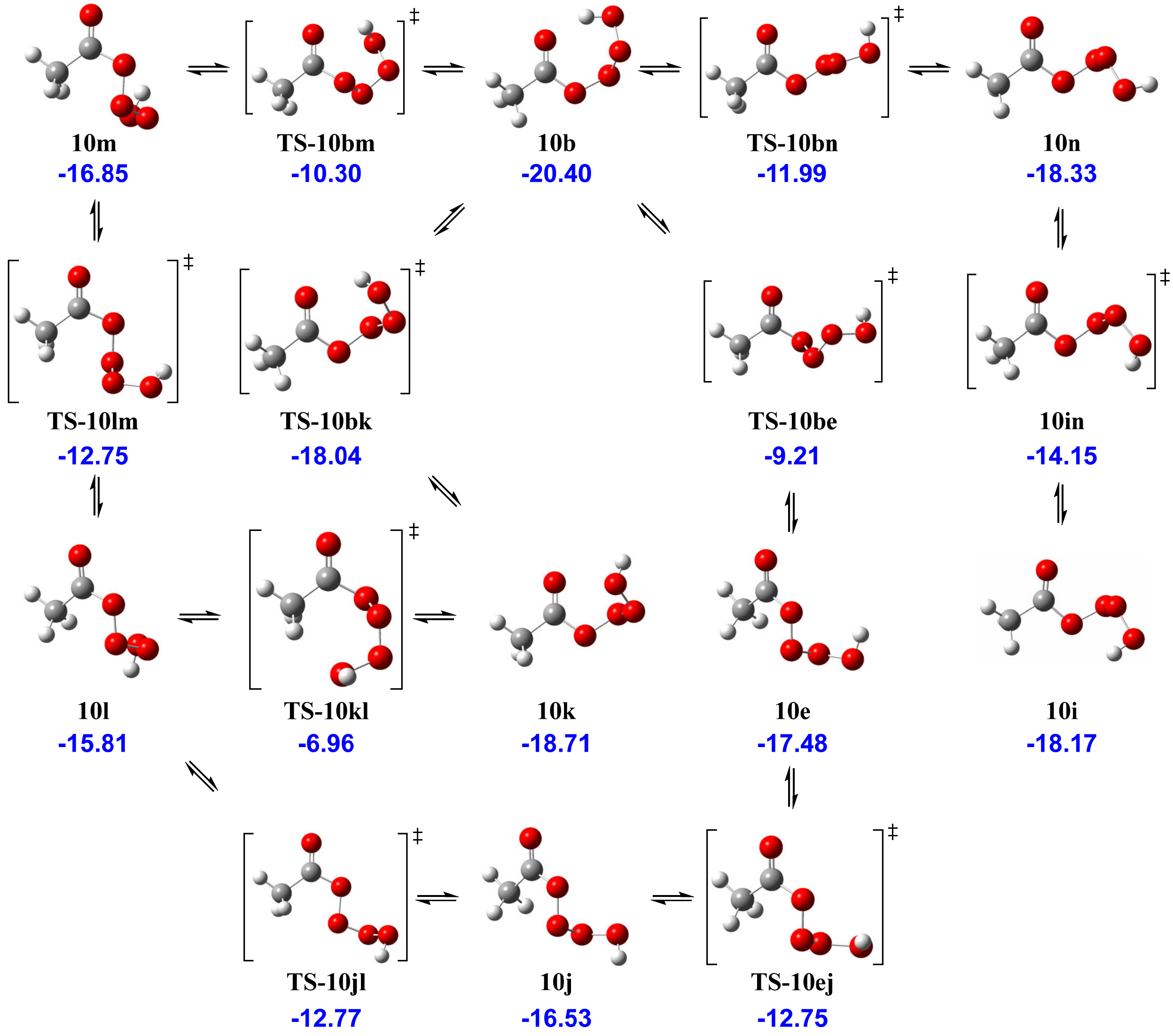

Figure 7. Hydrotetraoxide conformers and their interconversion transition structures. Energies (0 K, kcal mol^{-1}) in blue from W1BD//B3LYP calculations relative to the combined energies of *anti* acetylperoxy + HO_2.

Figure 8 presents our predictions for the rest of the reaction mechanism on the singlet surface.

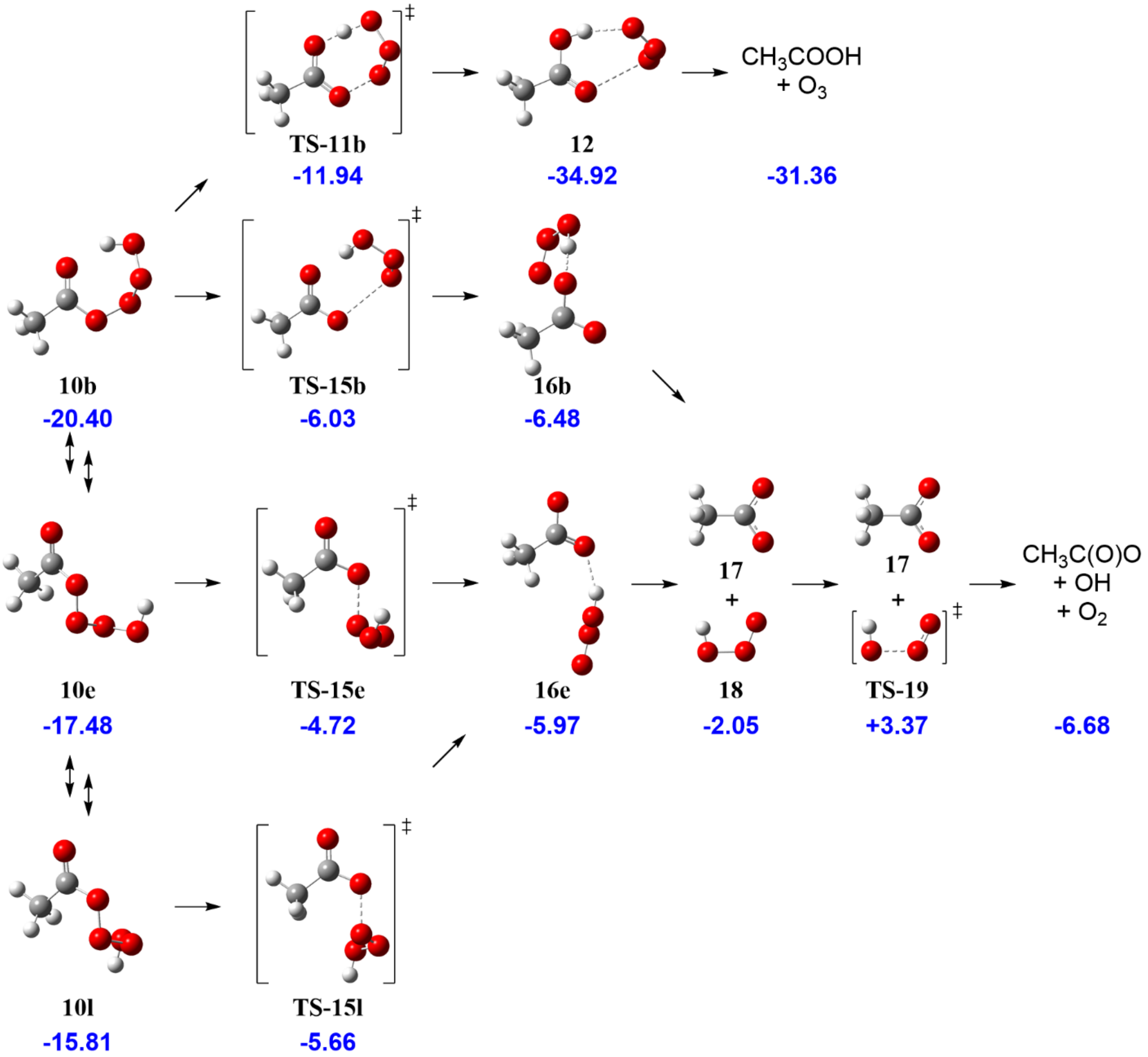

Figure 8. The singlet pathway for the acetylperoxy + HO_2 reaction from the hydrotetraoxide to either CH_3COOH + O_3 or to $CH_3C(O)O$ + OH + O_2. Energies (0 K, kcal mol^{-1}) in blue, relative to the combined energies of *anti* acetylperoxy + HO_2, calculated as described in the text. Double arrows denote that one or more structures have been omitted between the structures shown.

Of the eight conformers of the hydrotetraoxide, three undergo low-barrier chemical reactions. Only conformer **10b** has the requisite cyclic structure to undergo the 3,4-sigmatropic rearrangement (via **TS-11b**) previously described by Hasson et al.[9] The immediate product of the rearrangement is a hydrogen-bonded complex of acetic acid and ozone, **12**, that is 34.92 kcal mol^{-1} more stable than the original *anti* acetylperoxy + HO_2 reactants. Dissociation of **12** to the final CH_3COOH + O_3 products requires 3.56 kcal mol.

Conformers **10b**, **10e**, and **10l** are each capable of undergoing a low-barrier peroxy bond dissociation that ultimately leads to OH radical. (Peroxy bond dissociation in the other five conformers merely leads to interconversion to another hydrotetraoxide conformer.) Conformers **10b**, **10e**, and **10l** each pass through its own CO---OOOH dissociation transition structure (**TS-15b**, **TS-15e**, and **TS-15l**, respectively), forming one of two acetoxy-HO_3 radical pairs (**16b** or **16e**). The two radical pairs are within 0.5 kcal mol^{-1} of each other and ~6 kcal mol^{-1} more stable than the initial reactants. The ωB97X-D/cc-pVTZ+d geometry of the **TS-15b** saddle point coincides with the local maximum in the $E(\mathrm{OSS}) = {}^3E(\mathrm{W1BD}) + \Delta E_{\mathrm{SF}}$ energy. For the other two dissociation transition structures, we used the IRCMax approach[27] as described above. The energy of **TS-15e** was maximized at a reaction coordinate of $s = +2.72$ and the energy of **TS-15l** was maximized at $s = 1.40$.

After a barrierless dissociation of **16b** and **16e** into separated acetoxy (**17**) and HO_3 (**18**) radicals, HO_3 decomposes into OH and O_2. The most recent[63] high-level quantum chemical study of HO_3 isomerization and dissociation dynamics proposes that the barrier to *cis*-HO_3 dissociation is only 0.3 kcal mol^{-1}, thus submerging the TS directly responsible for OH formation below the energy of the original reactants. Therefore, it is reasonable to assume that HO_3 will be a stoichiometric source of OH under atmospheric conditions.

While the three reactive hydrotetraoxide conformers range in energy (relative to the original acetylperoxy + HO_2 reactants) from -20 to -16 kcal mol^{-1}, the peroxy bond dissociation transition structures range only from -6 to -5 kcal mol^{-1}. The weaker conformational preferences among **TS-15b**, **TS-15e**, and **TS-15l** is understandable given the rather large separation (~2 Å) between the acetoxy and HO_3 moieties.

The quantum chemical results in Figure 8 show that hydrotetraoxide rearrangement and decomposition to form CH_3COOH + O_3 has a significantly lower barrier than the serial dissociations that form $CH_3C(O)O$ + OH + O_2. However, the presence of three CO---OOOH dissociation channels provides OH formation an entropic advantage that O_3 formation lacks. In the statistical rate theory simulations presented below, we quantify the competition between these two product channels.

Statistical Rate Theory Results. *Triplet Mechanism*. Tables 1-3 present the RRKM/ME fractional yields and acetylperoxy + HO_2 rate coefficients, k_{trip}, at 298.15 K for each of the three triplet entrance channels of the mechanism represented in Figures 3 and 4 above. The one difference is that we did not include complexes **5b** and **5d**; we assumed that under simulations conditions the complexes would dissociate quantitatively to peracetic acid and triplet O_2. Following Weston et al.,[64] we compute the k_{trip} for a given bath gas pressure as the product of the capture rate constant, k_{cap}, for the formation of a given entrance channel complex (**3a**, **3f**, or **3h**) and the fraction of complex that goes on to form peracetic acid + O_2 (**6-*syn*** + **7** or **6-*anti*** + **7**). Using long-range transition state theory as described above,[43] we estimated a k_{cap} value of 1.84 x

10^{-9} cm^3 $molecule^{-1}$ s^{-1} for entrance channel complexes **3a** and **3f** and a value of 1.69 x 10^{-9} cm^3 $molecule^{-1}$ s^{-1} for **3h**.

Tables 1, 2, and 3 show that almost the entire nascent pre-reactive complex population falls apart to its immediate precursors; that is, **3a** and **3f** fall apart to re-form **1-*syn* + 2**, while **3h** falls apart to re-form **1-*anti* + 2**. That is, there is negligible interconversion of **1-*syn*** and **1-*anti*** induced by the HO_2 reaction. For pressures as high as 760 Torr, there is no predicted collisional stabilization of any of the pre-reactive complexes.

TABLE 1: RRKM/ME Yields and Triplet Rate Coefficients at 298 K for the Triplet Reaction Pathway Initiated by Formation of Complex 3a[a]

pressure (Torr)	**1-*syn* + 2**	**1-*anti* + 2**	**6-*syn* + 7**	**6-*anti* + 7**	k_{trip}[b]
1	0.9930	9.44×10^{-5}	0.006900	2.3×10^{-7}	1.27×10^{-11}
10	0.9930	9.31×10^{-5}	0.006897	2.3×10^{-7}	1.27×10^{-11}
20	0.9930	9.45×10^{-5}	0.006898	1.8×10^{-7}	1.27×10^{-11}
30	0.9930	9.43×10^{-5}	0.006903	3.2×10^{-7}	1.27×10^{-11}
40	0.9930	9.51×10^{-5}	0.006919	3.2×10^{-7}	1.27×10^{-11}
50	0.9930	9.29×10^{-5}	0.006922	2.8×10^{-7}	1.27×10^{-11}
100	0.9930	9.36×10^{-5}	0.006944	2.1×10^{-7}	1.27×10^{-11}
200	0.9929	9.46×10^{-5}	0.006985	2.0×10^{-7}	1.29×10^{-11}
300	0.9929	9.19×10^{-5}	0.007027	3.3×10^{-7}	1.29×10^{-11}
400	0.9929	9.34×10^{-5}	0.007052	3.0×10^{-7}	1.29×10^{-11}
500	0.9928	9.43×10^{-5}	0.007095	3.0×10^{-7}	1.31×10^{-11}
600	0.9928	9.36×10^{-5}	0.007155	2.6×10^{-7}	1.31×10^{-11}
700	0.9927	9.43×10^{-5}	0.007182	3.0×10^{-7}	1.32×10^{-11}
760	0.9927	9.46×10^{-5}	0.007199	3.1×10^{-7}	1.32×10^{-11}

[a] Simulations are of the mechanism in Figures 3 and 4. [b] In units of $\text{cm}^3\ \text{molecule}^{-1}\ \text{s}^{-1}$.

TABLE 2: RRKM/ME Yields and Triplet Rate Coefficients at 298 K for the Triplet Reaction Pathway Initiated by Formation of Complex 3f[a]

pressure (Torr)	**1-*syn* + 2**	**1-*anti* + 2**	**6-*syn* + 7**	**6-*anti* + 7**	k_{trip}[b]
1	0.9999	5.07×10^{-5}	2.0×10^{-6}	2×10^{-8}	9×10^{-14}
10	0.9999	5.02×10^{-5}	1.8×10^{-6}	1×10^{-8}	9×10^{-14}
20	0.9999	5.14×10^{-5}	1.8×10^{-6}	3×10^{-8}	9×10^{-14}
30	0.9999	5.08×10^{-5}	1.8×10^{-6}	6×10^{-8}	9×10^{-14}
40	0.9999	5.13×10^{-5}	1.7×10^{-6}	6×10^{-8}	9×10^{-14}
50	0.9999	5.11×10^{-5}	1.8×10^{-6}	1×10^{-8}	9×10^{-14}
100	0.9999	5.15×10^{-5}	1.9×10^{-6}	5×10^{-8}	9×10^{-14}
200	0.9999	5.14×10^{-5}	2.0×10^{-6}	4×10^{-8}	9×10^{-14}
300	0.9999	5.04×10^{-5}	1.7×10^{-6}	4×10^{-8}	9×10^{-14}
400	0.9999	5.21×10^{-5}	1.7×10^{-6}	1×10^{-8}	9×10^{-14}
500	0.9999	4.94×10^{-5}	2.0×10^{-6}	7×10^{-8}	9×10^{-14}
600	0.9999	5.14×10^{-5}	1.6×10^{-6}	8×10^{-8}	9×10^{-14}
700	0.9999	5.09×10^{-5}	1.7×10^{-6}	3×10^{-8}	9×10^{-14}
760	0.9999	5.13×10^{-5}	1.8×10^{-6}	3×10^{-8}	9×10^{-14}

[a] Simulations are of the mechanism in Figures 3 and 4. [b] In units of $\text{cm}^3\ \text{molecule}^{-1}\ \text{s}^{-1}$.

TABLE 3: RRKM/ME Yields and Triplet Rate Coefficients at 298 K for the Triplet Reaction Pathway Initiated by Formation of Complex 3h[a]

pressure (Torr)	**1-*syn* + 2**	**1-*anti* + 2**	**6-*syn* + 7**	**6-*anti* + 7**	k_{trip}[b]
1	1.06×10^{-4}	0.9998	3.9×10^{-6}	8.14×10^{-5}	1.7×10^{-13}
10	1.06×10^{-4}	0.9998	4.0×10^{-6}	8.16×10^{-5}	1.7×10^{-13}
20	1.05×10^{-4}	0.9998	3.9×10^{-6}	8.18×10^{-5}	1.7×10^{-13}
30	1.05×10^{-4}	0.9998	4.3×10^{-6}	8.20×10^{-5}	1.7×10^{-13}
40	1.07×10^{-4}	0.9998	4.2×10^{-6}	8.24×10^{-5}	1.7×10^{-13}
50	1.09×10^{-4}	0.9998	4.1×10^{-6}	8.14×10^{-5}	1.7×10^{-13}
100	1.06×10^{-4}	0.9998	4.1×10^{-6}	8.40×10^{-5}	1.7×10^{-13}
200	1.07×10^{-4}	0.9998	4.4×10^{-6}	8.27×10^{-5}	1.7×10^{-13}
300	1.06×10^{-4}	0.9998	3.9×10^{-6}	8.10×10^{-5}	1.7×10^{-13}
400	1.06×10^{-4}	0.9998	3.8×10^{-6}	8.08×10^{-5}	1.7×10^{-13}
500	1.07×10^{-4}	0.9998	4.3×10^{-6}	7.95×10^{-5}	1.7×10^{-13}
600	1.07×10^{-4}	0.9998	4.1×10^{-6}	8.19×10^{-5}	1.7×10^{-13}
700	1.07×10^{-4}	0.9998	3.6×10^{-6}	8.03×10^{-5}	1.7×10^{-13}
760	1.09×10^{-4}	0.9998	4.1×10^{-6}	8.18×10^{-5}	1.7×10^{-13}

[a] Simulations are of the mechanism in Figures 3 and 4. [b] In units of $\text{cm}^3\ \text{molecule}^{-1}\ \text{s}^{-1}$.

A comparison of Tables 1, 2, and 3 reveals that while reaction is slight along all three entrance channels, most of the triplet reactive flux passes through acetylperoxy-HO_2 complex **3a** (Figure 3). Conformer **3a** has to overcome a barrier of only 0.63 kcal mol^{-1} to interconvert to **3b** (Figure 4), which can undergo the hydrogen-transfer reaction via **TS-4b** to form final products. Reactivity upon formation of the other entrance channel complexes, **3f** and **3h**, is inhibited for two reasons. First, at least one relatively high interconversion TS (*i.e.*, a TS with an energy relative to **1-*anti* + 2** of ≥ 0 kcal mol^{-1}) blocks both **3f** and **3h** from accessing **TS-4b** (Figure 4 above). Second, **3f** and **3h** can readily access **TS-4d**, but this hydrogen-transfer TS is almost 4 kcal mol^{-1} higher in energy than **TS-4b**.

Table 1 shows that the rate coefficient for forming $CH_3C(O)OOH + O_2$ via the major entrance channel has a very slight pressure dependence, increasing from $k_{trip} = 1.27 \times 10^{-11}$ cm^3 molecule^{-1}s^{-1} at 100 Torr to $k_{trip} = 1.32 \times 10^{-11}$ cm^3 molecule^{-1}s^{-1} at 700 Torr. Higher pressures increase the rate of deactivation of the entrance channel complex, stabilizing it against reversion to reactants a bit. This ~4% increase in k_{trip} is significantly smaller than the uncertainties in Hui et al.'s measurements[4] of the triplet branching ratio, so we cannot comment on the accuracy of our predicted pressure dependence.

As Figure 3 indicates, the hydrogen transfer transition structure **TS-4b** is 4 kcal mol^{-1} lower in energy than the separated reactants. It may be surprising that such a large fraction (~99%) of entrance channel complexes decomposes back to separated acetylperoxy and HO_2, and that the fraction that goes forward over the hydrogen transfer barrier depends very little on pressure. However, there is precedence for this in the literature. For example, Yang, Sonk, and Barker,[65] in their computational study of the OH + OClO reaction, predicted the existence of a HOOClO adduct 8.68 kcal mol^{-1} below separated OH + OClO and a transition structure to form HOCl + $^1O_2$ 5.06

kcal mol^{-1} below separated OH + OClO. These authors predicted that at 298 K, ~90% of the HOOClO falls apart to OH + OClO, and that the fraction undergoing forward reaction varies insignificantly with pressure from 0.001 bar to 10 bar.

Tables 1S-21S summarize the same information presented in Tables 1-3 above for the other temperatures considered in this study. The key lesson from these additional tables is that as the temperature decreases, the fraction of pre-reactive complexes reverting to initial reactants also decreases, leading to a higher forward rate constant.

To compare our kinetics predictions for the triplet pathway more directly to experiment, we need a way to aggregate the simulation results in Tables 1, 2, and 3. Following Lei et al.,[66] we calculate the total triplet rate constant as the sum of the rate constant for each entrance channel weighted by the fractional population of the particular acetylperoxy reactant (either **1-*syn*** or **1-*anti***, Figure 3). Following the conventional labeling of reaction channels in equation 1 above, we denote the total triplet rate constant as k_{1a}. We computed the fractional populations assuming that the *syn* and *anti* forms of acetylperoxy were in thermal equilibrium. Table 4 shows these fractional populations, individual entrance-channel rate constants, and total rate constants as a function of temperatures found both in the troposphere and in the experiments of Hui et al.[4] Although the rate coefficient (in cm^3 molecule^{-1} s^{-1}) for reaction via entrance channel complex **3a** ranges from 3.23 x 10^{-11} at 230 K to 1.32 x 10^{-11} at 298.15 K, the total triplet rate constant is significantly lower because only 0.29 to 0.38 of the total population of acetylperoxy has a *syn* conformation over the temperatures studied.

TABLE 4: Individual Channel and Net Triplet Rate Coefficients at a Range of Tropospheric Temperatures

T (K)	*syn:anti*[a]	$k(\mathbf{3a})^b$	$k(\mathbf{3f})^b$	$k(\mathbf{3h})^b$	$k_{1a}{}^b$
230	0.286:0.714	3.23×10^{-11}	1.59×10^{-15}	2.16×10^{-13}	9.40×10^{-12}
240	0.301:0.699	2.80×10^{-11}	1.70×10^{-15}	2.10×10^{-13}	8.57×10^{-12}
250	0.316:0.684	2.41×10^{-11}	1.70×10^{-15}	2.02×10^{-13}	7.76×10^{-12}
260	0.329:0.671	2.12×10^{-11}	1.79×10^{-15}	1.91×10^{-13}	7.12×10^{-12}
270	0.342:0.658	1.85×10^{-11}	2.02×10^{-15}	1.85×10^{-13}	6.46×10^{-12}
280	0.355:0.645	1.63×10^{-11}	2.27×10^{-15}	1.79×10^{-13}	5.91×10^{-12}
290	0.366:0.634	1.45×10^{-11}	1.80×10^{-15}	1.66×10^{-13}	5.42×10^{-12}
298.15	0.375:0.625	1.32×10^{-11}	8.95×10^{-14}	1.67×10^{-13}	5.11×10^{-12}

[a] Relative abundances of the *syn* and *anti* conformers of acetylperoxy based on W1BD zero-point-corrected electronic energies and B3LYP/cc-pVTZ+d partition functions. [b] In units of $\mathrm{cm^3\ molecule^{-1}\ s^{-1}}$.

Finally, Hui et al.[4] have reported both the total rate constant, k_1, and the triplet branching fraction, α_{1a}, from 229 K to 294 K. By the definition of branching fraction, $k_{1a} = \alpha_{1a} k_1$. Figure 9 compares the experimental and the current theoretical values of k_{1a} as a function of temperature.

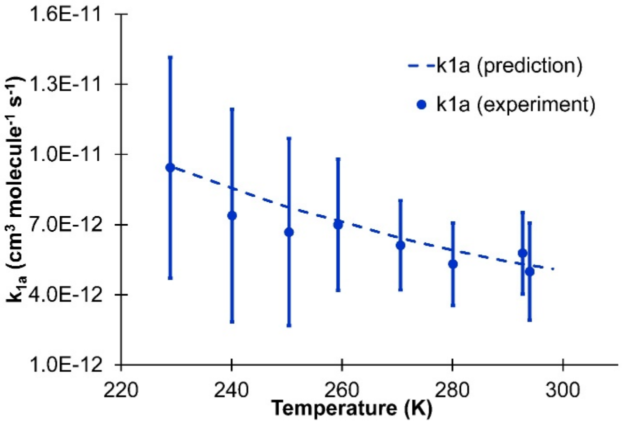

Figure 9. Comparing values of the triplet pathway rate constant from experiment[4] and from the current study. Error bars for the experimental rate constants propagated from those reported by Hui et al.[4] for the triplet branching fraction and for the total reaction rate constant.

Figure 9 shows excellent agreement between the experimental[4] and current theoretical rate constants for the triplet pathway across the range of temperatures relevant to the troposphere. This provides some validation of W1BD and our statistical rate theory approach, at least for this part of the reaction landscape.

However, the agreement between experiment and the current theoretical rate constants for the triplet pathway may be fortuitous. As mentioned above, a more thorough exploration of the van der Waals region of the potential energy surface might reveal that additional $CH_3C(O)OO$-HO_2 conformers (see Figure 4 above) are formed directly from separated $CH_3C(O)OO$ and HO_2. This could increase the predicted total triplet rate constant significantly. Moreover, direct formation of either **3b** or **3d** could, given their conformational similarity to **TS-4b** and **TS-4d**, respectively (see Figure 3 above) could accelerate the rate of the triplet reaction pathways. The validation of our theoretical approach must therefore be regarded as provisional.

Another issue to consider is the extent of energy randomization in the $CH_3C(O)OO$-HO_2 complexes. It is possible that the isomerization among these complexes (Figure 4 above) is driven only by energy stored in the intermolecular vibrational degrees of freedom. To test this idea, we repeated all of the above RRKM/ME simulations with only the intermolecular vibrational modes contributing to the sums and densities of states for the complexes and their isomerization transition states. Table 22S in the Supporting Information presents the individual channel and net triplet rate coefficients under these revised simulation assumptions. Table 22S also lists the percent change in the net triplet rate constants, k_{1a}, compared to those obtained assuming complete randomization of energy among all vibrational degrees of freedom (Table 4 above). Excluding the contributions from intramolecular vibrational modes increases the total triplet rate coefficients by 15-22% across the range of temperatures used in the simulations. This increase in predicted k_{1a} values somewhat lessens the agreement between experiment and theory compared to that shown in Figure 9 above; however, the rate constants in Table 22S still fall well within the error bars of the Hui et al.[4] measurements.

Singlet Mechanism. Tables 5-7 present the RRKM/ME fractional yields and acetylperoxy + HO_2 rate coefficients, k_{sing}, at 298.15 K for each of the three singlet entrance channels of the mechanism represented in Figures 6, 2S, 7 and 8 above. However, the ME simulations did not include structures **12**, **17**, **18**, or **TS-19**. That is, we assumed that under simulation conditions exit-channel complex **12** would dissociate quantitatively to acetic acid and ozone (we refer to this channel as "O_3" in the tables below) and that exit-channel complexes **16b** and **16e** would dissociate quantitatively to acetoxy, hydroxyl, and triplet molecular oxygen (we refer to this channel as "OH" in the tables below). Again, following Weston et al.,[64] we compute k_{sing} for a given bath gas pressure as the product of the capture rate constant, k_{cap}, for the formation of a given entrance channel complex (**8a**, **8f**, or **8h**) and the fraction of complex that forms a hydrotetraoxide (*e.g.* **10b**) or a subsequent structure in the mechanism. We used the same k_{cap} values for **1-*syn*** and ***1-anti*** stated above.

TABLE 5: RRKM/ME Yields and Singlet Rate Coefficients at 298 K for the Singlet Reaction Pathway Initiated by Formation of Complex 8a[a]

pressure (Torr)	**1-*syn* + 2**	**1-*anti* + 2**	**RO_4H**[b]	**O_3**	**OH**	k_{sing}[c]
1	0.9965	3.30×10^{-5}	0	1.38×10^{-3}	2.09×10^{-3}	6.37×10^{-12}
10	0.9965	3.21×10^{-5}	0	1.38×10^{-3}	2.09×10^{-3}	6.38×10^{-12}
20	0.9965	3.21×10^{-5}	0	1.38×10^{-3}	2.09×10^{-3}	6.38×10^{-12}
30	0.9965	3.19×10^{-5}	0	1.39×10^{-3}	2.09×10^{-3}	6.39×10^{-12}
40	0.9965	3.16×10^{-5}	1.00×10^{-8}	1.40×10^{-3}	2.08×10^{-3}	6.40×10^{-12}
50	0.9965	3.24×10^{-5}	1.00×10^{-8}	1.40×10^{-3}	2.07×10^{-3}	6.38×10^{-12}
100	0.9965	3.39×10^{-5}	3.70×10^{-7}	1.42×10^{-3}	2.07×10^{-3}	6.42×10^{-12}
200	0.9965	3.13×10^{-5}	4.37×10^{-6}	1.47×10^{-3}	2.02×10^{-3}	6.43×10^{-12}
300	0.9965	3.29×10^{-5}	1.61×10^{-5}	1.51×10^{-3}	1.98×10^{-3}	6.45×10^{-12}
400	0.9965	3.15×10^{-5}	3.44×10^{-5}	1.54×10^{-3}	1.94×10^{-3}	6.46×10^{-12}
500	0.9964	3.20×10^{-5}	6.25×10^{-5}	1.57×10^{-3}	1.91×10^{-3}	6.50×10^{-12}
600	0.9964	3.22×10^{-5}	9.60×10^{-5}	1.58×10^{-3}	1.88×10^{-3}	6.53×10^{-12}
700	0.9964	3.10×10^{-5}	1.33×10^{-4}	1.59×10^{-3}	1.84×10^{-3}	6.55×10^{-12}
760	0.9964	3.05×10^{-5}	1.57×10^{-4}	1.59×10^{-3}	1.81×10^{-3}	6.54×10^{-12}

[a] Simulations are of the mechanism in Figures 6, 7, 8, and 2S. [b] Total yield of collisionally stabilized hydrotetraoxides. [c] In units of cm^3 $molecule^{-1}$ s^{-1}.

TABLE 6: RRKM/ME Yields and Singlet Rate Coefficients at 298 K for the Singlet Reaction Pathway Initiated by Formation of Complex 8f[a]

pressure (Torr)	**1-*syn* + 2**	**1-*anti* + 2**	**RO_4H**[b]	**O_3**	**OH**	k_{sing}[c]
1	0.9999	7.85×10^{-6}	0	5.10×10^{-5}	7.79×10^{-5}	2.35×10^{-13}
10	0.9999	7.70×10^{-6}	0	5.12×10^{-5}	7.74×10^{-5}	2.35×10^{-13}
20	0.9999	7.25×10^{-6}	0	5.20×10^{-5}	7.82×10^{-5}	2.38×10^{-13}
30	0.9999	7.13×10^{-6}	0	5.27×10^{-5}	7.70×10^{-5}	2.37×10^{-13}
40	0.9999	8.14×10^{-6}	0	5.38×10^{-5}	7.81×10^{-5}	2.41×10^{-13}
50	0.9999	7.37×10^{-6}	0	5.55×10^{-5}	7.95×10^{-5}	2.46×10^{-13}
100	0.9999	7.58×10^{-6}	3.00×10^{-8}	5.74×10^{-5}	7.84×10^{-5}	2.48×10^{-13}
200	0.9998	7.58×10^{-6}	3.30×10^{-7}	6.35×10^{-5}	7.86×10^{-5}	2.60×10^{-13}
300	0.9998	7.28×10^{-6}	1.57×10^{-6}	6.90×10^{-5}	7.94×10^{-5}	2.74×10^{-13}
400	0.9998	7.22×10^{-6}	3.16×10^{-6}	7.34×10^{-5}	7.87×10^{-5}	2.84×10^{-13}
500	0.9998	7.36×10^{-6}	5.35×10^{-6}	7.87×10^{-5}	7.86×10^{-5}	2.97×10^{-13}
600	0.9998	7.32×10^{-6}	7.45×10^{-6}	8.28×10^{-5}	7.76×10^{-5}	3.07×10^{-13}
700	0.9998	7.36×10^{-6}	1.11×10^{-5}	8.39×10^{-5}	7.88×10^{-5}	3.17×10^{-13}
760	0.9998	7.48×10^{-6}	1.35×10^{-5}	8.57×10^{-5}	7.82×10^{-5}	3.24×10^{-13}

[a] Simulations are of the mechanism in Figures 6, 7, 8, and 2S. [b] Total yield of collisionally stabilized hydrotetraoxides. [c] In units of cm^3 $molecule^{-1}$ s^{-1}.

TABLE 7: RRKM/ME Yields and Singlet Rate Coefficients at 298 K for the Singlet Reaction Pathway Initiated by Formation of Complex 8h[a]

pressure (Torr)	**1-*syn* + 2**	**1-*anti* + 2**	**RO_4H**[b]	**O_3**	**OH**	k_{sing}[c]
1	3.40×10^{-5}	0.9980	0	5.07×10^{-4}	1.48×10^{-3}	3.37×10^{-12}
10	3.53×10^{-5}	0.9980	0	5.14×10^{-4}	1.48×10^{-3}	3.37×10^{-12}
20	3.46×10^{-5}	0.9980	0	5.14×10^{-4}	1.48×10^{-3}	3.37×10^{-12}
30	3.45×10^{-5}	0.9980	2.00×10^{-8}	5.19×10^{-4}	1.48×10^{-3}	3.39×10^{-12}
40	3.40×10^{-5}	0.9980	0	5.23×10^{-4}	1.49×10^{-3}	3.40×10^{-12}
50	3.38×10^{-5}	0.9980	3.00×10^{-8}	5.33×10^{-4}	1.48×10^{-3}	3.40×10^{-12}
100	3.46×10^{-5}	0.9980	4.60×10^{-7}	5.45×10^{-4}	1.46×10^{-3}	3.39×10^{-12}
200	3.39×10^{-5}	0.9979	5.66×10^{-6}	5.82×10^{-4}	1.44×10^{-3}	3.42×10^{-12}
300	3.48×10^{-5}	0.9979	1.90×10^{-5}	6.05×10^{-4}	1.41×10^{-3}	3.45×10^{-12}
400	3.40×10^{-5}	0.9979	4.10×10^{-5}	6.23×10^{-4}	1.39×10^{-3}	3.47×10^{-12}
500	3.43×10^{-5}	0.9979	6.98×10^{-5}	6.38×10^{-4}	1.36×10^{-3}	3.50×10^{-12}
600	3.36×10^{-5}	0.9979	1.02×10^{-4}	6.38×10^{-4}	1.34×10^{-3}	3.51×10^{-12}
700	3.38×10^{-5}	0.9979	1.36×10^{-4}	6.34×10^{-4}	1.31×10^{-3}	3.52×10^{-12}
760	3.39×10^{-5}	0.9979	1.61×10^{-4}	6.36×10^{-4}	1.30×10^{-3}	3.55×10^{-12}

[a] Simulations are of the mechanism in Figures 6, 7, 8, and 2S. [b] Total yield of collisionally stabilized hydrotetraoxides. [c] In units of cm^3 $molecule^{-1}$ s^{-1}.

Tables 5, 6, and 7 reveal that, like the triplet complexes, almost the entire nascent population of a given singlet pre-reactive complex falls apart to its immediate precursors; there is negligible interconversion of the *syn* and *anti* forms of the acetylperoxy reactant. For pressures as high as 760 Torr, there is no predicted collisional stabilization of any of the pre-reactive complexes, contrary to the earlier prediction of Hasson et al.[9] Simulations initiated by formation of **8a** reveal a slight (~3%) pressure dependence in rate constant that is significantly smaller than the uncertainty of any experimental rate measurements.

A comparison of Tables 5, 6, and 7 indicates that all three entrance channels, which involve the formation of complexes **8a**, **8f**, and **8h**, make non-negligible contributions to the total singlet reactive flux. This is unlike the triplet reactive flux, which proceeds almost exclusively through entrance channel complex **3a** (Table 1 above). The difference in reactivity arises from the differences in the barrier heights encountered at the first irreversible steps in the singlet and triplet mechanisms. For the singlet surface, the two tetraoxide formation transition structures, **TS-9b** and **TS-9e**, are close to -5 and -4 kcal mol^{-1} relative to the combined energies of the initial **1-*anti* + 2** reactants (Figure 6 above). These TS energies are low enough to allow multiple conformers of the singlet pre-reactive complex to go on to further reaction. In contrast, as discussed above, on the triplet surface, peracetic acid + O_2 formation happens almost exclusively through **TS-4b** since **TS-4d** is 4 kcal mol^{-1} higher in energy (Figure 3 above).

Tables 8, 9, and 10 disaggregate the total OH yield into contributions from the three transition structures responsible for OH formation, **TS-15b**, **TS-15e**, and **TS-15l**. Table 8 shows the results when pre-reactive complex **8a** is the simulation's initial well, Table 9 is for **8f** as the initial well, and Table 10 is for **8h** as the initial well.

TABLE 8: RRKM/ME Yields of OH Formed via TS-15b, TS-15e, and TS-15l in Simulations Initiated by Formation of Pre-Reactive Singlet Complex 8a[a]

pressure (Torr)	via **TS-15b**	via **TS-15e**	via **TS-15l**
1	1.97×10^{-3}	1.07×10^{-5}	1.10×10^{-4}
10	1.97×10^{-3}	1.14×10^{-5}	1.12×10^{-4}
20	1.97×10^{-3}	1.10×10^{-5}	1.10×10^{-4}
30	1.97×10^{-3}	1.12×10^{-5}	1.11×10^{-4}
40	1.96×10^{-3}	1.18×10^{-5}	1.12×10^{-4}
50	1.95×10^{-3}	1.06×10^{-5}	1.09×10^{-4}
100	1.95×10^{-3}	1.10×10^{-5}	1.09×10^{-4}
200	1.91×10^{-3}	1.10×10^{-5}	1.06×10^{-4}
300	1.87×10^{-3}	1.05×10^{-5}	1.04×10^{-4}
400	1.83×10^{-3}	1.08×10^{-5}	1.03×10^{-4}
500	1.80×10^{-3}	1.03×10^{-5}	9.87×10^{-5}
600	1.77×10^{-3}	9.81×10^{-6}	9.80×10^{-5}
700	1.74×10^{-3}	9.46×10^{-6}	9.24×10^{-5}
760	1.71×10^{-3}	9.26×10^{-6}	9.28×10^{-5}

[a] Simulations are of the mechanism in Figures 6, 7, 8, and 2S.

TABLE 9: RRKM/ME Yields of OH Formed via TS-15b, TS-15e, and TS-15l in Simulations Initiated by Formation of Pre-Reactive Singlet Complex 8f[a]

pressure (Torr)	via **TS-15b**	via **TS-15e**	via **TS-15l**
1	7.08×10^{-5}	1.04×10^{-6}	6.15×10^{-6}
10	7.03×10^{-5}	9.80×10^{-7}	6.17×10^{-6}
20	7.06×10^{-5}	9.70×10^{-7}	6.59×10^{-6}
30	6.98×10^{-5}	9.60×10^{-7}	6.19×10^{-6}
40	7.11×10^{-5}	1.04×10^{-6}	6.00×10^{-6}
50	7.23×10^{-5}	8.00×10^{-7}	6.38×10^{-6}
100	7.12×10^{-5}	1.00×10^{-6}	6.15×10^{-6}
200	7.17×10^{-5}	8.50×10^{-7}	6.11×10^{-6}
300	7.22×10^{-5}	7.90×10^{-7}	6.36×10^{-6}
400	7.13×10^{-5}	9.80×10^{-7}	6.49×10^{-6}
500	7.15×10^{-5}	9.50×10^{-7}	6.22×10^{-6}
600	7.10×10^{-5}	9.70×10^{-7}	5.62×10^{-6}
700	7.18×10^{-5}	1.14×10^{-6}	5.88×10^{-6}
760	7.09×10^{-5}	9.60×10^{-7}	6.28×10^{-6}

[a] Simulations are of the mechanism in Figures 6, 7, 8, and 2S.

TABLE 10: RRKM/ME Yields of OH Formed via TS-15b, TS-15e, and TS-15l in Simulations Initiated by Formation of Pre-Reactive Singlet Complex 8h[a]

pressure (Torr)	via **TS-15b**	via **TS-15e**	via **TS-15l**
1	5.59×10^{-4}	1.23×10^{-4}	8.02×10^{-4}
10	5.58×10^{-4}	1.22×10^{-4}	8.00×10^{-4}
20	5.53×10^{-4}	1.22×10^{-4}	8.04×10^{-4}
30	5.58×10^{-4}	1.23×10^{-4}	8.04×10^{-4}
40	5.57×10^{-4}	1.23×10^{-4}	8.07×10^{-4}
50	5.56×10^{-4}	1.22×10^{-4}	7.99×10^{-4}
100	5.42×10^{-4}	1.20×10^{-4}	7.98×10^{-4}
200	5.26×10^{-4}	1.20×10^{-4}	7.89×10^{-4}
300	5.08×10^{-4}	1.20×10^{-4}	7.86×10^{-4}
400	4.91×10^{-4}	1.19×10^{-4}	7.78×10^{-4}
500	4.71×10^{-4}	1.18×10^{-4}	7.74×10^{-4}
600	4.54×10^{-4}	1.16×10^{-4}	7.66×10^{-4}
700	4.37×10^{-4}	1.18×10^{-4}	7.55×10^{-4}
760	4.35×10^{-4}	1.15×10^{-4}	7.50×10^{-4}

[a] Simulations are of the mechanism in Figures 6, 7, 8, and 2S.

The first thing to note is that in all three sets of simulations, **TS-15e** is responsible for the least OH yield. This is a consequence of **TS-15e**'s being 1 kcal mol^{-1} higher in energy than **TS-15b** and **TS-15l** (Figure 8 above). In simulations initiated with **8a** and **8f**, more than 90% of the OH comes via **TS-15b**, while in simulations initiated with **8h**, more than 50% of the OH comes via **TS-15l**. This reactivity is consistent with the quantum chemistry presented above. Figure S2 in the Supporting Information shows that conformers **8a** and **8f** both readily access conformer **8b**, which is reasonable since all of these conformers have synperiplanar C=O and O-O bonds. Structure **8b**, in turn, directly leads to **TS-9b** and hydrotetraoxide **10b** (Figure 6 above) and **10b** is the direct precursor of **TS-15b** (Figure 8 above). In contrast, conformer **8h**, with antiperiplanar C=O and O-O bonds, does not readily rearrange to **8b**. Conformer **8h** does have a relatively low-barrier pathway to conformer **8e** (Figure S2 in the Supporting Information), which leads directly to **TS-9e** and hydrotetraoxide **10e** (Figure 6 above). Barriers of < 5 kcal mol^{-1} separate **10e** from **10l** (Figure 7 above) which is the direct precursor of **TS-15l**. Conformer **10e** does access the lowest-energy OH-forming **TS-15b** (Figure 8 above) to some extent, but the high barriers to *E-Z* interconversion lessen the contribution to this pathway.

We ran simulations with **8a**, **8f**, and **8h** at temperatures ranging from 230 to 290 K (data not shown). As we found with our triplet simulations, one clear trend as temperature decreases is decreasing reversion of the singlet pre-reactive complexes to acetylperoxy + HO_2, thus leading to higher reaction rate constants.

Table 11 presents the aggregation of singlet rate constants for each of the three entrance channels across the array of temperatures in our study, again following the procedure of Lei et al.[66] Note that each of the rate constants in Table 11 includes contributions from both the O_3-forming pathway (reaction 1b above) and the OH-forming pathway (reaction 1c above). Thus, to conform to existing notation, we denote the total singlet rate constant as k_{1b+1c}.

TABLE 11: Individual Channel and Net Singlet Rate Coefficients at a Range of Tropospheric Temperatures

T (K)	*syn:anti*[a]	$k(8\mathbf{a})$[b]	$k(\mathbf{8f})$[b]	$k(\mathbf{8h})$[b]	k_{1b+1c}[b]
230	0.286:0.714	1.75×10^{-11}	1.06×10^{-12}	8.39×10^{-12}	1.13×10^{-11}
240	0.301:0.699	1.49×10^{-11}	8.66×10^{-13}	7.25×10^{-12}	9.81×10^{-12}
250	0.316:0.684	1.28×10^{-11}	7.18×10^{-13}	6.32×10^{-12}	8.59×10^{-12}
260	0.329:0.671	1.10×10^{-11}	5.99×10^{-13}	5.51×10^{-12}	7.52×10^{-12}
270	0.342:0.658	9.53×10^{-12}	5.05×10^{-13}	4.85×10^{-12}	6.63×10^{-12}
280	0.355:0.645	8.29×10^{-12}	4.23×10^{-13}	4.31×10^{-12}	5.87×10^{-12}
290	0.366:0.634	7.22×10^{-12}	3.63×10^{-13}	3.85×10^{-12}	5.22×10^{-12}
298.15	0.375:0.625	6.54×10^{-12}	3.24×10^{-13}	3.55×10^{-12}	4.79×10^{-12}

[a]Relative amounts of the *syn* and *anti* conformers of acetylperoxy based on W1BD zero-point-corrected electronic energies and B3LYP/cc-pVTZ+d partition functions. [b]In units of cm^3 $molecule^{-1}$ s^{-1}.

As already noted, the total singlet rate constants (in cm^3 $molecule^{-1}$ s^{-1}) have a negative temperature dependence, with the rate constant at 230 K, $k_{1b+1c} = 1.13 \times 10^{-11}$, being a factor of 2.3 larger than $k_{1b+1c} = 4.79 \times 10^{-12}$ at 298.15 K. All three entrance channels contribute significantly to the total singlet rate constant at all temperatures and in fact, although the intrinsically fastest reaction is initiated by formation of complex **8a**, reactive flux flowing through complex **8h** makes the largest contribution to the total singlet reactive flux because of the significantly higher relative population of the *anti* acetylperoxy reactant that is the direct precursor of **8h**.

Hui et al.[4] have reported both the total rate constant, k_1, and the singlet branching fractions, α_{1b} and α_{1c}, from 229 K to 294 K. By the definition of branching fraction, $k_{1b+1c} = (\alpha_{1b} + \alpha_{1c}) k_1$. Figure 10 compares the experimental and the new theoretical values of k_{1b+1c} as a function of temperature.

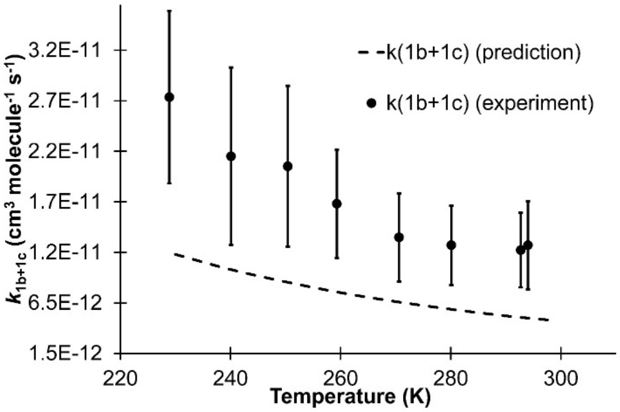

Figure 10. Comparing values of the combined singlet pathways rate constant from experiment[4] and from the current study. Error bars for the experimental rate constants propagated from those reported by Hui et al.[4] for the branching fractions of reactions 1b and 1c and for the total reaction rate constant.

Figure 10 reveals a large negative systematic error in the predicted singlet rate constants, with the predictions ranging from a factor of 2.0 to a factor of 2.6 lower than the experimental rate constants. Our underprediction of k_{1b+1c} would necessarily cause us to overpredict the triplet branching fraction, α_{1a}, as well.

We improved the agreement between the predicted and experimental singlet rate by performing an *ad hoc* adjustment in which we increased the energies of **1-*syn*** and **1-*anti*** (Figure 6 above), the two conformers of the original acetylperoxy. Qualitatively, the effect of such an adjustment is to increase the chemical activation of all minima on the singlet potential energy surface, which in turn increases the probability that the singlet pre-reactive complexes will go on to reaction via pathways 1b and 1c instead of reverting to reactants, increasing the predicted rate constant.

Quantitatively, we found that increasing the energies of **1-*syn*** and **1-*anti*** each by 0.9 kcal mol^{-1} provided the best agreement of predicted and experimental[4] singlet rate constants across the range of temperatures under consideration. Table 12 contains the revised predictions of individual channel and net rate coefficients and Figure 11 compares the revised predictions to the experimental values.

One underlying reason that the singlet potential energy surface, without any adjustment to the amount of chemical activation, leads to singlet rate constants that are too low may be an incomplete characterization of the van der Waals region of the potential energy surface. As discussed above, there may be additional $CH_3C(O)OO$-HO_2 conformers (see Figure S2) that are formed directly from separated $CH_3C(O)OO$ and HO_2. This has the potential of increasing the total singlet rate constant significantly. Moreover, direct formation of either **8b** or **8e** could, given their conformational similarity to **TS-9b** and **TS-9e**, respectively (see Figure S2 and Figure 6 above) could accelerate the rate of hydrotetraoxide formation, which would lead in turn to faster formation of $CH_3COOH + O_3$ and $CH_3C(O)O + OH + O_2$ products. A more accurate treatment of the formation of singlet $CH_3C(O)OO$-HO_2 complexes could therefore reduce the magnitude of the *ad hoc* adjustment to the chemical activation energy needed to bring the predicted total singlet rate constant into agreement with experiment.

With the predicted rates for both the triplet pathway and the combined singlet pathways now established to be reliable, we are in a position to consider branching fractions for the acetylperoxy + HO_2 reaction.

TABLE 12: Individual Channel and Net Singlet Rate Coefficients at a Range of Tropospheric Temperatures with All Singlet Structures Given 0.9 kcal mol^{-1} More Energy

T (K)	*syn:anti*[a]	k(8**a**)[b]	k(**8f**)[b]	k(**8h**)[b]	k_{1b+1c}[b]
230	0.286:0.714	3.83×10^{-11}	3.97×10^{-12}	2.36×10^{-11}	2.89×10^{-11}
240	0.301:0.699	3.29×10^{-11}	3.24×10^{-12}	2.04×10^{-11}	2.52×10^{-11}
250	0.316:0.684	2.84×10^{-11}	2.66×10^{-12}	1.78×10^{-11}	2.19×10^{-11}
260	0.329:0.671	2.45×10^{-11}	2.21×10^{-12}	1.55×10^{-11}	1.92×10^{-11}
270	0.342:0.658	2.13×10^{-11}	1.84×10^{-12}	1.36×10^{-11}	1.68×10^{-11}
280	0.355:0.645	1.86×10^{-11}	1.55×10^{-12}	1.20×10^{-11}	1.49×10^{-11}
290	0.366:0.634	1.62×10^{-11}	1.31×10^{-12}	1.07×10^{-11}	1.32×10^{-11}
298.15	0.375:0.625	1.47×10^{-11}	1.17×10^{-12}	9.75×10^{-12}	1.20×10^{-11}

[a] Relative amounts of the *syn* and *anti* conformers of acetylperoxy based on W1BD zero-point-corrected electronic energies and B3LYP/cc-pVTZ+d partition functions. [b] In units of cm^3 molecule^{-1} s^{-1}.

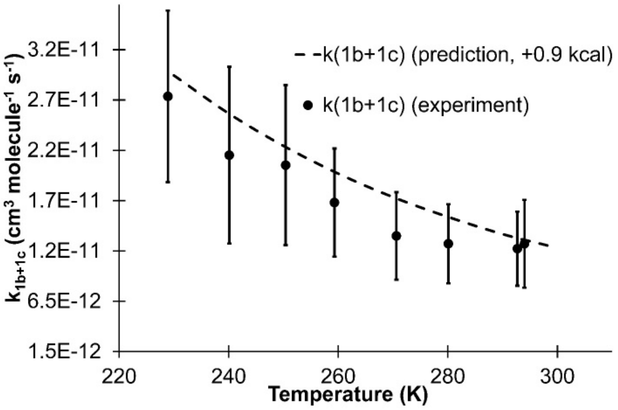

Figure 11. Comparing values of the combined singlet pathways rate constant from experiment[4] and from the current study, with all singlet structures possessing 0.9 kcal mol^{-1} of additional energy. Error bars for the experimental rate constants propagated from those reported by Hui et al.[4] for the branching fractions of reactions 1b and 1c and for the total reaction rate constant.

Branching Ratios. As discussed above, our simulations do not predict pressure dependences in rate constants of more than a few percent across the range of tropospherically relevant pressures. Thus, all of the numerical results we present below will be at 760 Torr.

As presented in the Introduction, given the widely disparate atmospheric impacts of the three channels of the acetylperoxy + HO_2 reaction, a central focus of experimental studies has been measurement of the branching fractions for these channels:

$$CH_3C(O)OO + HO_2 \rightarrow CH_3C(O)OOH + O_2 \quad [1a]$$

$$CH_3C(O)OO + HO_2 \rightarrow CH_3C(O)OH + O_3 \quad [1b]$$

$$CH_3C(O)OO + HO_2 \rightarrow CH_3C(O)O + OH + O_2 \quad [1c]$$

Our RRKM/ME simulations predict only four statistically significant outcomes for the acetylperoxy + HO_2 system: $CH_3C(O)OOH$ (+ O_2) formation, O_3 (+ $CH_3C(O)OH$) formation, OH (+ O_2 + $CH_3C(O)O$) formation, and collisionally stabilized hydrotetraoxide (RO_4H) formation.

Table 13 summarizes our predicted yields and the total predicted rate constant, k_1, as a function of temperature. Figure 12 shows the three predicted branching ratios as a function of temperature, taking α_{1a} to be the yield of $CH_3C(O)OOH$, α_{1b} to be the combined yield of O_3 and thermalized RO_4H, and α_{1c} to be the yield of OH. (Since the barrier for the sigmatropic shift is much lower than the barrier for peroxy bond homolysis (Figure 8 above), we assume that stabilized RO_4H will isomerize quantitively to O_3 (+ $CH_3C(O)OH$) on a thermal time scale.)

The first thing to note is that the OH channel, reaction 1c, is the most important channel at all temperatures studied. At 298 K, α_{1c} has its maximum value of 0.461. This branching fraction decreases with temperature, reaching a value of 0.422 at 230 K. According to our mechanism, reaction 1c is the most entropically favored of the three reaction pathways, with three energetically accessible transition structures (**TS-15b**, **TS-15e**, and **TS-15l** in Figure 8) leading to product, while reactions 1a and 1b each have only one energetically accessible TS (**TS-4b** in Figure 3 and **TS-11b** in Figure 8, respectively). This entropic advantage of 1c decreases as the temperature decreases, consistent with the predicted decline in α_{1c}.

TABLE 13: Predicted Yields for the Acetylperoxy + HO_2 Reaction[a]

T (K)	$CH_3C(O)OOH$	O_3	RO_4H	OH	k_1[b]
230	0.245	0.333	1.29 x 10^{-3}	0.422	3.83 x 10^{-11}
240	0.254	0.316	9.48 x 10^{-4}	0.430	3.37 x 10^{-11}
250	0.261	0.301	9.37 x 10^{-4}	0.437	2.97 x 10^{-11}
260	0.271	0.287	9.23 x 10^{-4}	0.443	2.63 x 10^{-11}
270	0.277	0.275	9.14 x 10^{-4}	0.448	2.33 x 10^{-11}
280	0.284	0.262	9.04 x 10^{-4}	0.454	2.08 x 10^{-11}
290	0.292	0.251	8.94 x 10^{-4}	0.458	1.86 x 10^{-11}
298.15	0.298	0.241	8.85 x 10^{-4}	0.461	1.72 x 10^{-11}

[a] Simulation results based on singlet structures having 0.9 kcal mol^{-1} additional energy. [b] In units of cm^3 $molecule^{-1}$ s^{-1}.

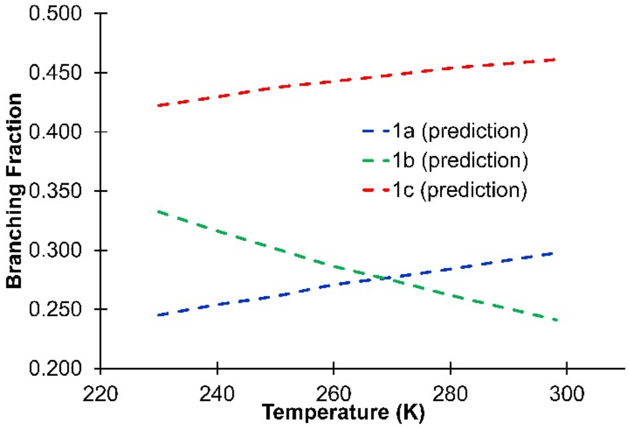

Figure 12. The current theoretical predictions of the branching fractions for the three channels of the acetylperoxy + HO_2 reaction with all singlet structures possessing 0.9 kcal mol^{-1} of additional energy.

The same decrease in temperature strongly favors the O_3 channel, with an increase in α_{1b} from 0.241 at 298.15K to 0.334 at 230 K, an increase of branching fraction of almost 40%. This is a consequence of the O_3 channel's having the lowest reaction barrier of all three channels. The $CH_3C(O)OOH$ channel decreases modestly with decreasing temperature: $\alpha_{1a} = 0.298$ at 298.15 K and 0.245 at 230 K, a 20% decrease. Finally, there is a strong negative temperature dependence of the overall rate constant, with k_1 at 230 K being 2.2 times larger than k_1 at 298.15 K. The predicted rate constant (in cm^3 $molecule^{-1}$ s^{-1}) at 298.15 K, 1.72×10^{-11}, is ~20% higher than the IUPAC[12] and JPL[13] recommended value of 1.4×10^{-11}.

At all temperatures, collisional stabilization to the tetraoxide is almost negligible; that is, virtually all products are formed promptly. This is consistent with multiple experiments observing roughly the same branching fractions on different time scales.[4-8]

Finally, Figure 13a, b, and c compare experiment and current theory for each of the three branching fractions. Figure 13a shows the branching fraction for reaction 1a, $CH_3C(O)OOH$ formation. It shows excellent agreement between the measurements of Hui et al.[4] and the current predictions across the temperature range studied. In contrast, the experimental branching fraction for reaction 1b, O_3 formation, increases far more rapidly with decreasing temperature than the current predictions, and the experimental branching fraction for reaction 1c, OH formation, decreases far more rapidly with decreasing temperature than the current predictions. An inaccurate prediction of the temperature dependence in the singlet branching fractions, α_{1b} and α_{1c}, but not in the triplet branching fraction, α_{1a}, may suggest specific significant electronic structure or statistical thermodynamic errors in our treatment of the rate-limiting transition states responsible for O_3 and OH formation, such as our neglect of anharmonicities in these highly dissociated structures.

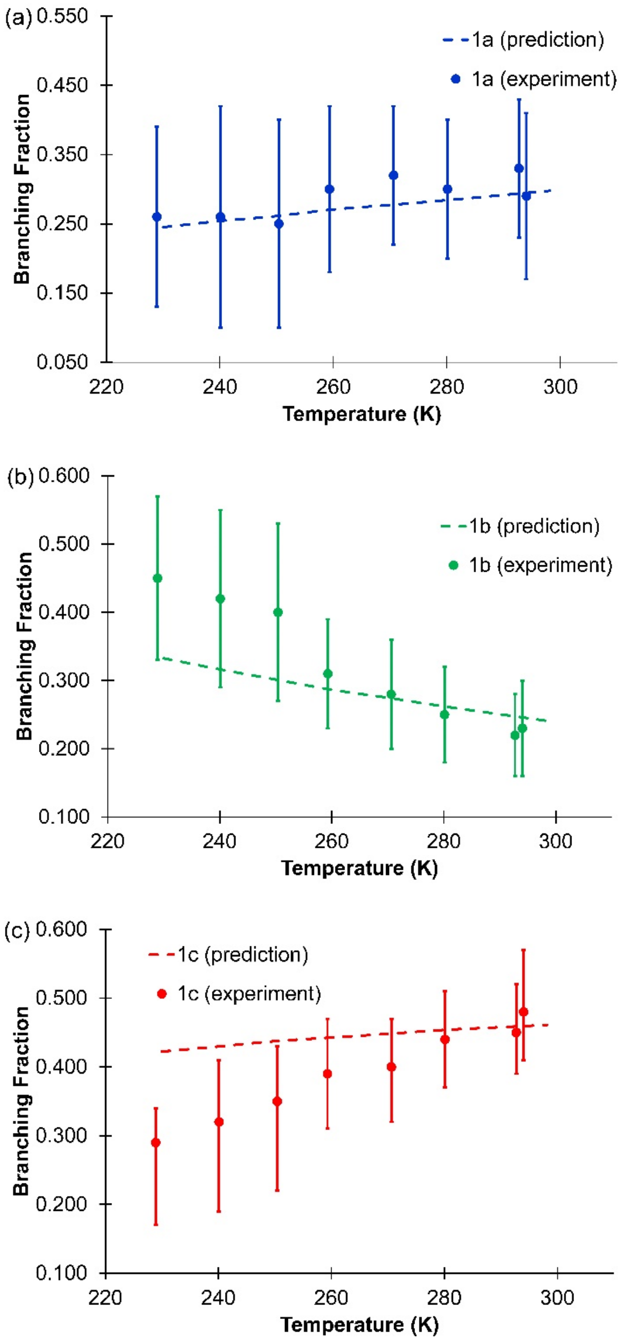

Figure 13. Comparing values of the branching fractions for the $CH_3C(O)OO + HO_2$ reaction from experiment[4] and from the current study, with all singlet structures possessing 0.9 kcal mol^{-1} of additional energy. (a) for channel 1a, (b) for channel 1b, (c) for channel 1c.

CONCLUSION

For the acetylperoxy + HO_2 reaction, our use of W1BD theory and explicit treatment of multiple conformers provided excellent agreement with experimental kinetics[4] for the triplet pathway, reaction 1a, leading to peracetic acid + O_2 products. For the singlet pathways, the use of spin-flip coupled-cluster theory as an affordable way to account for static electron correlation proved less successful. An *ad hoc* increase of 0.9 kcal mol^{-1} in the energy of all minima on the singlet surface was necessary to predict a total singlet rate constant in good agreement with experiment, and our theoretical predictions could not match the strong temperature dependence in the branching fractions for reactions 1b and 1c. Still, the theoretical approach employed here provides qualitatively reasonable predictions and may therefore be of use in the reaction of HO_2 with other carbonyl peroxy reactions capable of both hydroperoxide formation on the triplet surface and OH formation on the singlet surface.

CONFLICTS OF INTEREST

There are no conflicts to declare.

ACKNOWLEDGMENTS

The authors acknowledge support from the National Science Foundation (CHE-1412622 and CHE-2108202). M. P. D. also acknowledges a Beckman Scholars Award from the Arnold and Mabel Beckman Foundation. The authors used the computational facilities of the Midwest Undergraduate Computational Chemistry Consortium at Hope College (established by NSF grants CHE-0520704, CHE-1039925, and OAC-1919571) and the XSEDE facility at the University of California, San Diego (CHE-150037 and CHE-160060).

References

1. J. J. Orlando and G. S. Tyndall, *Chem. Soc. Rev.*, 2012, **41**, 6294-6317.
2. A. R. Russell, L. C. Valin and R. C. Cohen, *Atmos. Chem. Phys.*, 2012, **12**, 12197-12209.
3. M. E. Jenkin, R. Valorso, B. Aumont and A. R. Rickard, *Atmos. Chem. Phys.*, 2019, **19**, 7691-7717.
4. A. O. Hui, M. Fradet, M. Okumura and S. P. Sander, *J. Phys. Chem. A*, 2019, **123**, 3655-3671.
5. F. A. F. Winiberg, T. J. Dillon, S. C. Orr, C. B. M. Groß, I. Bejan, C. A. Brumby, M. J. Evans, S. C. Smith, D. E. Heard and P. W. Seakins, *Atmos. Chem. Phys.*, 2016, **16**, 4023-4042.
6. C. B. M. Groβ, T. J. Dillon, G. Schuster, J. Lelieveld and J. N. Crowley, *J. Phys. Chem. A*, 2014, **118**, 974-985.
7. M. E. Jenkin, M. D. Hurley and T. J. Wallington, *Phys. Chem. Chem. Phys.*, 2007, **9**, 3149-3162.
8. A. S. Hasson, G. S. Tyndall and J. J. Orlando, *J. Phys. Chem. A*, 2004, **108**, 5979-5989.
9. A. S. Hasson, K. T. Kuwata, M. C. Arroyo and E. B. Petersen, *J. Photoch. Photobio. A*, 2005, **176**, 218-230.
10. G. K. Moortgat, B. Veyret and R. Lesclaux, *Chem. Phys. Lett.*, 1989, **160**, 443-447.
11. J. A. Montgomery, Jr., M. J. Frisch, J. W. Ochterski and G. A. Petersson, *J. Chem. Phys.*, 1999, **110**, 2822-2827.
12. R. Atkinson, D. L. Baulch, R. A. Cox, J. N. Crowley, R. F. Hampson, R. G. Hynes, M. E. Jenkin, M. J. Rossi and J. Troe, *Atmos. Chem. Phys.*, 2006, **6**, 3625-4055.
13. J. B. Burkholder, S. P. Sander, J. Abbatt, J. R. Barker, C. Cappa, J. D. Crounse, T. S. Dibble, R. E. Huie, C. E. Kolb, M. J. Kurylo, V. L. Orkin, C. J. Percival, D. M. Wilmouth and P. H. Wine, *Chemical Kinetics and Photochemical Data for Use in Atmospheric Studies, Evaluation No. 19*, Jet Propulsion Laboratory, Pasadena2019.
14. E. C. Barnes, G. A. Petersson, J. A. Montgomery, M. J. Frisch and J. M. L. Martin, *J. Chem. Theory Comput.*, 2009, **5**, 2687-2693.
15. S. V. Levchenko and A. I. Krylov, *J. Chem. Phys.*, 2004, **120**, 175-185.
16. P. U. Manohar and A. I. Krylov, *J. Chem. Phys.*, 2008, **129**, 194105.
17. M. Kumar, J. Shee, B. Rudshteyn, D. R. Reichman, R. A. Friesner, C. E. Miller and J. S. Francisco, *J. Am. Chem. Soc.*, 2020, **142**, 10806-10813.
18. T. Kurtén and N. M. Donahue, *J. Phys. Chem. A*, 2012, **116**, 6823-6830.
19. K. H. Møller, K. H. Bates and H. G. Kjaergaard, *J. Phys. Chem. A*, 2019, **123**, 920-932.
20. A. D. Becke, *J. Chem. Phys.*, 1993, **98**, 5648-5652.
21. C. Lee, W. Yang and R. G. Parr, *Phys. Rev. B*, 1988, **37**, 785-789.
22. T. H. Dunning, *J. Chem. Phys.*, 1989, **90**, 1007-1023.
23. J. M. L. Martin and G. d. Oliveira, *J. Chem. Phys.*, 1999, **111**, 1843-1856.
24. L. Noodleman, *J. Chem. Phys.*, 1981, **74**, 5737-5743.
25. D. R. Glowacki, S. P. Marsden and M. J. Pilling, *J. Am. Chem. Soc.*, 2009, **131**, 13896-13897.
26. M. K. Sprague and K. K. Irikura, *J. Phys. Chem. A*, 2015, **119**, 7052-7062.
27. D. K. Malick, G. A. Petersson and J. A. Montgomery, Jr., *J. Chem. Phys.*, 1998, **108**, 5704-5713.

28. I. M. Alecu, J. Zheng, Y. Zhao and D. G. Truhlar, *J. Chem. Theory Comput.*, 2010, **6**, 2872-2887.
29. J.-D. Chai and M. Head-Gordon, *Phys. Chem. Chem. Phys.*, 2008, **10**, 6615-6620.
30. N. Mardirossian and M. Head-Gordon, *Mol. Phys.*, 2017, **115**, 2315-2372.
31. M. Pfeifle, Y.-T. Ma, A. W. Jasper, L. B. Harding, W. L. Hase and S. J. Klippenstein, *J. Chem. Phys.*, 2018, **148**, 174306.
32. K. T. Kuwata, E. J. Guinn, M. R. Hermes, J. A. Fernandez, J. M. Mathison and K. Huang, *J. Phys. Chem. A*, 2015, **119**, 10316-10335.
33. A. I. Krylov, *Acc. Chem. Res.*, 2006, **39**, 83-91.
34. A. I. Krylov, *Annu. Rev. Phys. Chem.*, 2008, **59**, 433-462.
35. P. U. Manohar, J. F. Stanton and A. I. Krylov, *J. Chem. Phys.*, 2009, **131**, 114112.
36. M. J. Frisch, G. W. Trucks, H. B. Schlegel, G. E. Scuseria, M. A. Robb, J. R. Cheeseman, G. Scalmani, V. Barone, G. A. Petersson, H. Nakatsuji, X. Li, M. Caricato, A. V. Marenich, J. Bloino, B. G. Janesko, R. Gomperts, B. Mennucci, H. P. Hratchian, J. V. Ortiz, A. F. Izmaylov, J. L. Sonnenberg, D. Williams-Young, F. Ding, F. Lipparini, F. Egidi, J. Goings, B. Peng, A. Petrone, T. Henderson, D. Ranasinghe, V. G. Zakrzewski, J. Gao, N. Rega, G. Zheng, W. Liang, M. Hada, M. Ehara, K. Toyota, R. Fukuda, J. Hasegawa, M. Ishida, T. Nakajima, Y. Honda, O. Kitao, H. Nakai, T. Vreven, K. Throssell, J. A. Montgomery Jr., J. E. Peralta, F. Ogliaro, M. J. Bearpark, J. J. Heyd, E. N. Brothers, K. N. Kudin, V. N. Staroverov, T. A. Keith, R. Kobayashi, J. Normand, K. Raghavachari, A. P. Rendell, J. C. Burant, S. S. Iyengar, J. Tomasi, M. Cossi, J. M. Millam, M. Klene, C. Adamo, R. Cammi, J. W. Ochterski, R. L. Martin, K. Morokuma, O. Farkas, J. B. Foresman and D. J. Fox, Wallingford, CT2016.
37. Y. Shao, Z. Gan, E. Epifanovsky, A. T. B. Gilbert, M. Wormit, J. Kussmann, A. W. Lange, A. Behn, J. Deng, X. Feng, D. Ghosh, M. Goldey, P. R. Horn, L. D. Jacobson, I. Kaliman, R. Z. Khaliullin, T. Kuś, A. Landau, J. Liu, E. I. Proynov, Y. M. Rhee, R. M. Richard, M. A. Rohrdanz, R. P. Steele, E. J. Sundstrom, H. L. Woodcock, P. M. Zimmerman, D. Zuev, B. Albrecht, E. Alguire, B. Austin, G. J. O. Beran, Y. A. Bernard, E. Berquist, K. Brandhorst, K. B. Bravaya, S. T. Brown, D. Casanova, C.-M. Chang, Y. Chen, S. H. Chien, K. D. Closser, D. L. Crittenden, M. Diedenhofen, R. A. DiStasio, H. Do, A. D. Dutoi, R. G. Edgar, S. Fatehi, L. Fusti-Molnar, A. Ghysels, A. Golubeva-Zadorozhnaya, J. Gomes, M. W. D. Hanson-Heine, P. H. P. Harbach, A. W. Hauser, E. G. Hohenstein, Z. C. Holden, T.-C. Jagau, H. Ji, B. Kaduk, K. Khistyaev, J. Kim, J. Kim, R. A. King, P. Klunzinger, D. Kosenkov, T. Kowalczyk, C. M. Krauter, K. U. Lao, A. D. Laurent, K. V. Lawler, S. V. Levchenko, C. Y. Lin, F. Liu, E. Livshits, R. C. Lochan, A. Luenser, P. Manohar, S. F. Manzer, S.-P. Mao, N. Mardirossian, A. V. Marenich, S. A. Maurer, N. J. Mayhall, E. Neuscamman, C. M. Oana, R. Olivares-Amaya, D. P. O'Neill, J. A. Parkhill, T. M. Perrine, R. Peverati, A. Prociuk, D. R. Rehn, E. Rosta, N. J. Russ, S. M. Sharada, S. Sharma, D. W. Small, A. Sodt, T. Stein, D. Stück, Y.-C. Su, A. J. W. Thom, T. Tsuchimochi, V. Vanovschi, L. Vogt, O. Vydrov, T. Wang, M. A. Watson, J. Wenzel, A. White, C. F. Williams, J. Yang, S. Yeganeh, S. R. Yost, Z.-Q. You, I. Y. Zhang, X. Zhang, Y. Zhao, B. R. Brooks, G. K. L. Chan, D. M. Chipman, C. J. Cramer, W. A. Goddard, M. S. Gordon, W. J. Hehre, A. Klamt, H. F. Schaefer, M. W. Schmidt, C. D. Sherrill, D. G. Truhlar, A. Warshel, X. Xu, A. Aspuru-Guzik, R. Baer, A. T. Bell, N. A. Besley, J.-D. Chai, A. Dreuw, B. D. Dunietz, T. R. Furlani, S. R. Gwaltney, C.-P. Hsu, Y. Jung, J. Kong, D. S. Lambrecht, W. Liang, C. Ochsenfeld, V. A. Rassolov, L. V. Slipchenko, J. E. Subotnik, T. Van

Voorhis, J. M. Herbert, A. I. Krylov, P. M. W. Gill and M. Head-Gordon, *Mol. Phys.*, 2014, **113**, 184-215.

38. J. R. Barker, T. L. Nguyen, J. F. Stanton, C. Aieta, M. Ceotto, F. Gabas, T. J. D. Kumar, C. G. L. Li, L. L. Lohr, A. Maranzana, N. F. Ortiz, J. M. Preses, J. M. Simmie, J. A. Sonk and P. J. Stimac, University of Michigan, Ann Arbor, MI2019.
39. J. R. Barker, *Int. J. Chem. Kinet.*, 2009, **41**, 748-763.
40. J. R. Barker, *Int. J. Chem. Kinet.*, 2001, **33**, 232-245.
41. P. J. Robinson and K. A. Holbrook, *Unimolecular Reactions*, Wiley-Interscience, London, 1972.
42. K. T. Kuwata, L. Luu, A. B. Weberg, K. Huang, A. J. Parsons, L. A. Peebles, N. B. Rackstraw and M. J. Kim, *J. Phys. Chem. A*, 2018, **122**, 2485-2502.
43. Y. Georgievskii and S. J. Klippenstein, *J. Chem. Phys.*, 2005, **122**, 194103.
44. E. D. Glendening, A. E. Reed, J. E. Carpenter and F. Weinhold, University of Wisconsin, Madison, WI1998.
45. L. A. Curtiss, P. C. Redfern, K. Raghavachari, V. Rassolov and J. A. Pople, *J. Chem. Phys.*, 1999, **110**, 4703-4709.
46. P. L. Fast, M. L. Sanchez and D. G. Truhlar, *Chem. Phys. Lett.*, 1999, **306**, 407-410.
47. F. M. Mourits and F. H. A. Rummens, *Can. J. Chem.*, 1977, **55**, 3007-3020.
48. H. Hippler, J. Troe and H. J. Wendelken, *J. Chem. Phys.*, 1983, **78**, 6709-6717.
49. D. W. McCann and R. P. Danner, *Ind. Eng. Chem. Process Des. Dev.*, 1984, **23**, 529-533.
50. K. G. Joback and R. C. Reid, *Chem. Eng. Comm.*, 1987, **57**, 233-243.
51. R. C. Reid, J. M. Prausnitz and B. E. Poling, *The Properties of Gases and Liquids*, McGraw-Hill, New York, 1987.
52. J. O. Hirschfelder, C. F. Curtiss and R. B. Bird, *Molecular Theory of Gases and Liquids*, Wiley, New York, 1954.
53. K. T. Kuwata, L. C. Valin and A. D. Converse, *J. Phys. Chem. A*, 2005, **109**, 10710-10725.
54. J. R. Barker, L. M. Yoder and K. D. King, *J. Phys. Chem. A*, 2001, **105**, 796-809.
55. N. Snider, *J. Chem. Phys.*, 1984, **80**, 1885-1893.
56. S. Grimme, J. Antony, S. Ehrlich and H. Krieg, *J. Chem. Phys.*, 2010, **132**, 154104.
57. R. A. Kendall, T. H. D. Jr. and R. J. Harrison, *J. Chem. Phys.*, 1992, **96**, 6796-6806.
58. A. E. Reed, R. B. Weinstock and F. Weinhold, *J. Chem. Phys.*, 1985, **83**, 735-746.
59. J. W. Ochterski, G. A. Petersson and J. A. Montgomery, Jr., *J. Chem. Phys.*, 1996, **104**, 2598-2619.
60. B. Sirjean, R. Fournet, P. A. Glaude and M. F. Ruiz-Lopez, *Chem. Phys. Lett.*, 2007, **435**, 152-156156.
61. D. M. Pawar, A. A. Khalil, D. R. Hooks, K. Collins, T. Elliott, J. Stafford, L. Smith and E. A. Noe, *J. Am. Chem. Soc.*, 1998, **120**, 2108-2112.
62. K. B. Wiberg, *J. Org. Chem.*, 2019, **84**, 10938-10945.
63. J. Zuo, Q. Chen, X. Hu, H. Guo and D. Xie, *J. Phys. Chem. A*, 2020, **124**, 6427-6437.
64. R. E. Weston, T. L. Nguyen, J. F. Stanton and J. R. Barker, *J. Phys. Chem. A*, 2013, **117**, 821-835.
65. L. Yang, J. A. Sonk and J. R. Barker, *J. Phys. Chem. A*, 2015, **119**, 5723-5731.
66. W. Lei, R. Zhang, W. S. McGivern, A. Derecskei-Kovacs and S. W. North, *J. Phys. Chem. A*, 2001, **105**, 471-477.